frontiers | Frontiers in Earth Science

TYPE Original Research
PUBLISHED 10 November 2022
DOI 10.3389/feart.2022.868011

Check for updates

OPEN ACCESS

EDITED BY
Melissa Ovedia Anderson,
University of Toronto, Canada

REVIEWED BY
Zhuyin Chu,
Institute of Geology and Geophysics (CAS), China
Kate Kiseeva,
University College Cork, Ireland

*CORRESPONDENCE
A. Bénard,
antoine.benard@unil.ch

SPECIALTY SECTION
This article was submitted to Petrology, a section of the journal Frontiers in Earth Science

RECEIVED 01 February 2022
ACCEPTED 05 September 2022
PUBLISHED 10 November 2022

CITATION
Bénard A (2022), Spinel harzburgite–derived silicate melts forming sulfide-bearing orthopyroxenite in the lithosphere. Part 2: Sulfide compositions and their chalcophile and highly siderophile trace element signatures.
Front. Earth Sci. 10:868011.
doi: 10.3389/feart.2022.868011

COPYRIGHT
© 2022 Bénard. This is an open-access article distributed under the terms of the Creative Commons Attribution License (CC BY). The use, distribution or reproduction in other forums is permitted, provided the original author(s) and the copyright owner(s) are credited and that the original publication in this journal is cited, in accordance with accepted academic practice. No use, distribution or reproduction is permitted which does not comply with these terms.

Spinel harzburgite–derived silicate melts forming sulfide-bearing orthopyroxenite in the lithosphere. Part 2: Sulfide compositions and their chalcophile and highly siderophile trace element signatures

A. Bénard*

Institute of Earth Sciences, University of Lausanne, Lausanne, Switzerland

In the first article, we have reported petrological data for a new, glass-bearing orthopyroxenite vein cutting a sub-arc mantle xenolith from Kamchatka. As similar veins from the West Bismarck arc, this orthopyroxenite is sulfide-rich and formed by cooling of parental melts derived by partial melting of spinel harzburgite sources. Here, I report new data for the abundances of major base metals and chalcophile and highly siderophile trace elements in vein sulfides from the two localities. Kamchatka vein sulfides are all Cu-poor monosulfide solid solution (MSS). West Bismarck veins contain MSS and a ternary (Fe, Cu, Ni)S solid solution ("xSS"), which ranges between MSS and intermediate solid solution (ISS) in composition. Sulfides follow Ni and Cu enrichment trends and have chondrite-normalized platinum-group element (PGE) patterns with elevated Pt relative to Os, Ir, Ru, and Rh. Pt alloys are frequently associated with sulfides and vugs formed from hydrothermal fluids, which also contain metallic Fe and wüstite. Vein sulfides, ranging from Fe-rich MSS (ca. 1,050–1,100°C) to xSS (≤850°C) through Ni-rich MSS, were formed in a sulfide liquid line of descent under oxygen and sulfur fugacity conditions (fO_2 and fS_2) down to one log unit below the fayalite–magnetite–quartz and close to the Pt-PtS buffers, respectively. The Ni and Cu enrichment trends in MSS are consistent with cooling and fractionation of Ni-rich and Cu-poor sulfide liquids (original atomic ∑metal/S~0.9), which will finally solidify as xSS or ISS. Chondrite-normalized Pt/Pd>1 in some of the sulfides is a signature of spinel harzburgite sources. Because it occurs at relatively low fS_2, the crystallization sequence of these sulfide liquids is accompanied by the formation of abundant PGE alloys and other metallic phases. Melts derived from spinel harzburgite sources can be originally oxidized to carry up to ~2,600 ppm S (predominantly as S^{6+}) and follow a sulfide-undersaturated evolution trend, until they are rapidly cooled to crystallize as orthopyroxenite dykes or sills. There, S^{6+}-Fe^{2+} redox reactions with host

rocks, together with the production of high-Mg# andesite derivatives with low S solubility and high-temperature, hydrothermal fluids at decreasing fO_2 and fS_2, will lead to the local precipitation of abundant sulfides and alloys.

KEYWORDS

sub-arc mantle, low-Ca boninite, harzburgite, partial melting, sulfide, base metal, chalcophile trace element, highly siderophile trace element

Introduction

The sources of subduction zone magmas generated in the asthenospheric mantle wedge are thought to be modified by a combination of 1) ancient melt depletion events in different tectonic settings; and 2) fluxing (or "hybridization") by volatile-rich melts and/or fluids derived from the subducted lithosphere ("slab agents"), which may lead to a higher oxidation state than that recorded by mid-ocean ridge basalts (MORB; Arculus and Powell, 1986; Kessel et al., 2005; Wallace, 2005; Kelley and Cottrell, 2009; Evans et al., 2012; Nebel et al., 2015; Foden et al., 2018; Bénard et al., 2016; Bénard et al., 2017a; Bénard et al., 2017b; Bénard et al., 2018a; Bénard et al., 2018b; Bénard et al., 2021).

Boninites are magnesian, basaltic andesite and andesite magmas usually found at subduction zones. These magmas have been classified according to a CaO/Al_2O_3 threshold of 0.75, which distinguishes high-Ca (HCB) from low-Ca (LCB) boninites and is believed to primarily indicate the transition from spinel-bearing, depleted lherzolite to harzburgite mantle sources (Crawford et al., 1989). The major and trace element compositional ranges of volatile-rich boninites do suggest that they derive from sources that have experienced ancient melt extraction events (Jenner, 1981; Hickey and Frey, 1982; Cameron et al., 1983; Crawford et al., 1989; Taylor et al., 1994; Sobolev and Chaussidon, 1996; Bédard, 1999; Le Bas et al., 2000; Kamenetsky et al., 2002; Reagan et al., 2009; Cooper et al., 2010; König et al., 2010; Pearce and Raegan, 2019; Coulthard et al., 2021). Furthermore, studies of sub-arc mantle peridotites have shown that both HCB and LCB endmember can be characterized by high volatile contents and an elevated oxidation state at a primitive stage (Bénard et al., 2016; Bénard et al., 2017b; Bénard et al., 2018b; Bénard et al., 2018c; Bénard et al., 2022). However, large variations in volatile contents and oxidation state are sometimes observed in boninites sampled on the ocean floor, even though they are not as primitive as those in mantle peridotites (Brounce et al., 2015; Brounce et al., 2021).

Enrichments in highly incompatible lithophile trace elements in both HCB and LCB are widely believed to commonly originate from high degrees of melting of depleted mantle sources, fluxed by slab agents (e.g., König et al., 2010). Those high melting degrees (F) should range above ~25% to account for clinopyroxene exhaustion in spinel lherzolite, under hydrous conditions and at ≤1.2 GPa (Gaetani and Grove, 1998; Bénard et al., 2021). Underpinning this model is the hypothesis that extraction of LCB occurs after HCB in a continuous mantle depletion and fluxing process. However, recent studies of sulfide-bearing orthopyroxenite veins formed from LCB in mantle peridotites from the Kamchatka and West Bismarck (Papua New Guinea) arcs have shed new light on some of the contrasting aspects of HCB versus LCB petrogenesis (Bénard and Ionov, 2012; Bénard and Ionov, 2013; Bénard et al., 2016; Bénard et al., 2018c; Bénard et al., 2022). These studies have notably outlined that LCB melt batches can be produced independently of HCB by low-degree melting (F≤5%) of spinel harzburgite. These results agree with both experimental and modeling data in support of a melt productivity decrease by a factor of ~4 at the lherzolite–harzburgite mantle source transition, for a given set of pressure–temperature (P-T) conditions (Klingenberg and Kushiro, 1996; Hirschmann et al., 1999; Falloon and Danyushevsky, 2000; Parman and Grove, 2004). Such F variations (i.e., from ≥25% to ≤5%) can have a profound impact on the incompatible element compositions of LCB, including volatiles and Fe^{3+}. Furthermore, the orthopyroxenite veins were shown to record wide variations in the oxidation state, from relatively oxidized ($\Delta\log fO_2$[FMQ]~+1.5) to more reduced conditions similar to MORB (−1≤$\Delta\log fO_2$[FMQ]≤0; e.g., Berry et al., 2018), where fO_2 and FMQ refer to oxygen fugacity and the fayalite-magnetite-quartz oxygen buffer, respectively (Bénard and Ionov, 2012; Bénard and Ionov, 2013; Bénard et al., 2018a; Bénard et al., 2018c; Bénard et al., 2022). This fO_2 range notably corresponds to the interval where S^{2-} transitions to S^{6+} in silicate melts (Jugo et al., 2010; Klimm et al., 2012), which has profound implications for the transport of sulfur and chalcophile elements in magmas (e.g., Botcharnikov et al., 2011).

Sulfur in boninites has raised interest in the past because it has been proposed that early sulfide undersaturation in such "second-stage" melts (i.e., melts derived from sources that have experienced prior melt extraction events) could be responsible for their elevated platinum-group element (PGE) endowments, particularly Pt and Pd (PPGE) on which these models were originally based (Hamlyn and Keays, 1986; Keays, 1995). Indeed, despite being primarily classified as highly siderophile, PGE also have a strong affinity for S^{2-} dissolved in silicate melts (Laurenz et al., 2013) or in sulfide liquids (Mungall and Brenan, 2014). Since Hamlyn and Keays (1986), technical progress has allowed the analyses of chalcophile and highly siderophile trace elements with greater accuracy and precision in boninites, further

supporting that these magmas are undersaturated in sulfide at relatively low-P conditions (e.g., on the ocean floor; Woodland et al., 2002; Dale et al., 2012; Valetich et al., 2019; Brounce et al., 2021). However, neither PPGE enrichments nor sulfide undersaturation are specific to boninites under these low-P conditions. Instead, these two features are rather common for many subduction zone magmas (e.g., Park et al., 2012, Park et al., 2013), in contrast with MORB (Mungall and Brenan, 2014; Smythe et al., 2017). Furthermore, sulfide undersaturation can also be produced during second-stage magma differentiation processes, since decompression and/or higher fO_2 increase S solubility in basaltic melts (Mavrogenes and O'Neill, 1999; Botcharnikov et al., 2011). Therefore, an initial sulfide undersaturation state during boninite genesis in the mantle remains to be identified.

Rare studies of boninite-derived cumulates formed at high pressure have also suggested the early crystallization of refractory Os-Ir-Ru (IPGE) alloys from these magmas (Peck et al., 1992). This further raises questions about how fO_2 evolves in primitive boninites, since the solubility of PGE alloys in silicate melts are strong positive functions of this parameter (e.g., Brenan et al., 2005). Under low fO_2 conditions, sulfide liquid saturation could be expected during the high-P evolution of boninites, since sulfide solubility limits in Fe-poor andesitic melts are much lower than in Fe-rich basalts (Mavrogenes and O'Neill 1999; Bénard et al., 2022). Once sulfide liquid saturation is reached, sulfide solid solutions can form during cooling (e.g., Fleet et al., 1993; Fleet and Pan, 1994; Ballhaus et al., 2001; Mungall et al., 2005; Zhang and Hirschmann, 2016). The timing of sulfide saturation in boninites has been constrained to occur at an earlier stage (i.e., after less fractionation) than in typical ridge basalt, as inferred from chalcophile element systematics of melt inclusions (MI) formed at relatively low pressure in these magmas (e.g., Valetich et al., 2019). However, the compositional range of such solid sulfide phases has not been reported so far, assuming that they can form among other high-P crystallization products of boninites.

In this context, the sulfide-rich nature of the orthopyroxenite veins from the Kamchatka and West Bismarck arcs appears to be of interest. At first glance, this feature could either be related to an elevated sulfur (S) concentration rate (i.e., $F \leq 5\%$) or the ingress of S-rich slab agents (i.e., $F \geq 25\%$) during the partial melting events forming the orthopyroxenite original melts, depending therefore on the preferred model for LCB genesis. Sulfur appears as a moderately incompatible element during mantle melting at $\Delta \log fO_2[\text{FMQ}] \sim 0$, since its concentration varies from ~250 ppm in the primitive mantle (PM; McDonough and Sun, 1995) to ~119 ppm in the depleted MORB mantle (DMM; Salters and Stracke, 2004). Spinel harzburgites formed by $F \geq 25\%$ at ≤3 GPa (i.e., the putative sources of LCB) cannot contain more than ~50 ppm S, provided that no post-melting metasomatism occurred (Lorand et al., 2013). However, many studies have suggested that slab agents can deliver and transport significant amounts of sulfur to the mantle wedge (e.g., Alt et al., 2012; Jégo and Dasgupta, 2013, Jégo and Dasgupta, 2014; Tomkins and Evans, 2015), though controversy on this point has been raised recently (Li et al., 2020). A relationship between slab sulfur and mantle wedge fO_2 has also been suggested because of the potential of S^{6+} to act as an oxidizer of Fe^{2+} in igneous rocks. Highly soluble sulfate species transported from the slab in Fe-poor silicic melts and/or serpentine fluids have notably been considered as key oxidizing agents able to raise mantle wedge fO_2 (Alt et al., 2012; Klimm et al., 2012; Prouteau and Scaillet, 2012; Debret and Sverjensky, 2017; Bénard et al., 2018b). However, the intrinsic fO_2 of deserpentinization fluids is also controversial (Piccoli et al., 2019; Maurice et al., 2020). Studying sulfides in primitive veins formed from LCB and recording variable fO_2 can therefore help in understanding a variety of key topics linking mantle wedge melting with volatile evolution and the behavior of precious metals.

Here, I report the first data for major base metals and chalcophile and highly siderophile trace elements in vein sulfides from the Kamchatka and West Bismarck sub-arc mantles. I used these data to 1) estimate the parental sulfide liquid compositions; 2) further constrain fO_2 and sulfur fugacity (fS_2) during sulfide formation; and 3) discuss the precious metal potential of LCB through sulfide and alloy precipitation.

Samples and main inferences from part 1

The Kamchatka xenoliths in this study (samples Av20 and Av55; Bénard and Ionov, 2012; Bénard and Ionov, 2013; Bénard et al., 2017b; Bénard et al., 2022) were sampled from recent volcanic ash (low-K, basaltic andesite and andesite of subalkaline affinity), on the western slope of the active Avacha volcano. Avacha is located ~30 km northwest of the city of Petropavlosk-Kamchatsky, near the middle of the volcanic chain that makes up Kamchatka's eastern volcanic front (Ionov, 2010). The West Bismarck xenolith in this study (sample 67-02E(3); Bénard et al., 2018c) was recovered from an active, submarine cinder cone (low-K picrite of subalkaline affinity) laying within the debris field northwest of the partially collapsed Ritter volcano. The Ritter volcano is located between Umboi and Sakar near the volcanic front of the arc, ~20 km west of New Britain (Bénard et al., 2018c). Further details about the sample collection and the geological and tectonic setting of the Kamchatka and West Bismarck arcs can be found in the studies mentioned before.

All xenoliths are veined, coarse-grained spinel harzburgites with protogranular micro-structures, which originate from the sub-arc mantle lithosphere (Ionov, 2010). Samples were selected according to the classifications established by Bénard and Ionov (2012) and Bénard and Ionov (2013) for the veins in Kamchatka samples, which was later used by Bénard et al. (2018c) for those from West Bismarck. Here, I concentrate on the "rapidly-crystallized" veins (i.e., fringe-bearing; "Type 1A"), which were

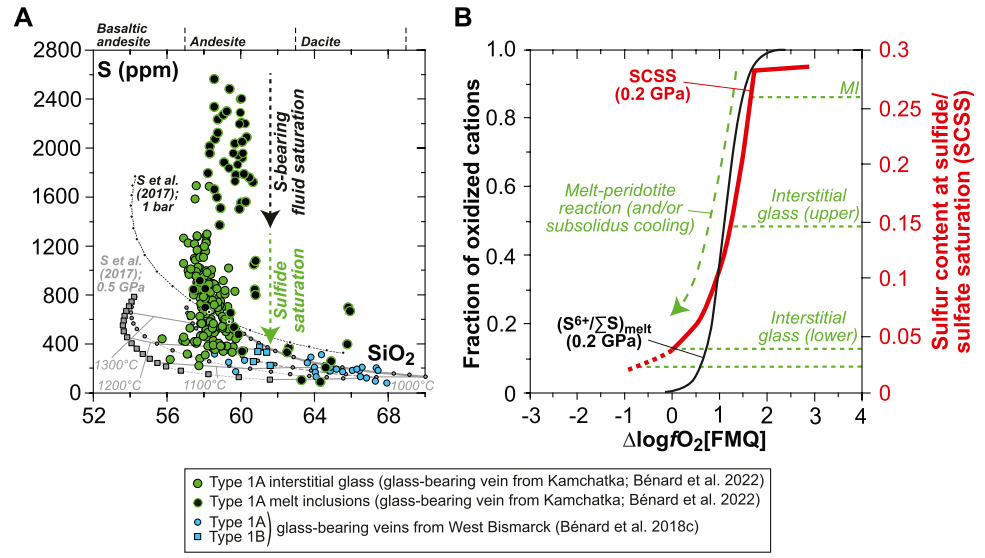

FIGURE 1
Sulfur composition and inferred $S^{6+}/\sum S$ ($S^{6+}/(S^{6+}+S^{2-})$) in silicate melts for the glass-bearing Type 1A veins from Kamchatka and Type 1A and Type 1B veins from West Bismarck (Bénard et al., 2018c; Bénard et al., 2022). **(A)** S abundances measured by EPMA and SEM in vein MI and interstitial glass plotted against SiO_2 (in wt%). Also, SCSS calculated with the model of Smythe et al. (2017) at 1 bar and 0.5 GPa (black and gray lines, respectively) are shown. Melt major element compositions used to calculate SCSS are those of isobaric models for the liquid lines of descent of spinel harzburgite–derived melts (i.e., LCB) at 1 GPa, calculated by Bénard et al. (2018c) with pMELTS (Ghiorso et al., 2002). **(B)** Plot of $S^{6+}/\sum S$ in silicate melts ($S^{6+}/\sum S_{melt}$; black curves) against $\Delta\log fO_2$[FMQ]. The $S^{6+}/\sum S_{melt}$ curves are derived from experiments at 0.2 GPa (Jugo et al., 2010; Klimm et al., 2012). Also shown in **(B)** are the SCSS in experimental andesitic melt at 0.2 GPa (red curve; Botcharnikov et al., 2011) and the highest S abundances measured in the MI, as well as the upper- and lower-end S abundances measured in the interstitial glass from the Kamchatka vein (dotted green lines; Bénard et al., 2022). The decrease in S abundances from MI to the interstitial glass is triggered by S capture in high-T, hydrothermal fluids, and magmatic sulfide saturation, concomitant with a decrease in the oxidation state from $\Delta\log fO_2$[FMQ]~+1.5 to $-1\leq\Delta\log fO_2$[FMQ]≤ 0 due to a S^{6+}-Fe^{2+} redox exchange during melt-rock reactions (dotted and dashed arrows in **(A)** and **(B)**).

recognized as being formed from the most primitive parental LCB melts (Bénard and Ionov, 2012; Bénard and Ionov, 2013; Bénard et al., 2018c; Bénard et al., 2022). All samples contain silicate glass, apart from sample Av20, which is composed of orthopyroxene (opx) and sulfides, as well as minor amphibole and spinel. The compositional features of the silicate glass, either found interstitially or as opx-hosted MI, was notably used in earlier studies to track volatile evolution during vein formation (e.g., S; Bénard et al., 2018c; Bénard et al., 2022).

In the first article of this two-part study, we have shown that the original LCB melts of the sulfide-bearing orthopyroxenite veins were mainly transporting sulfur as S^{6+}-bearing species ($\Delta\log fO_2$[FMQ]~+1.5), with up to ~2,600 ppm S in the opx-hosted MI (Figure 1A; Bénard et al., 2022). Upon melt intrusion in the sub-arc mantle lithosphere, the exsolution of high-T, S-bearing hydrothermal fluids, shortly after (or concurrently with) sulfide liquid crystallization, was triggered in the veins as the result of elevated undercooling degrees. Cooling of the vein parental melts also resulted in the formation and quenching of high-Mg# (Mg#=Mg/(Mg+Fe_t) where Fe_t indicates all Fe treated as Fe^{2+}) andesite and dacite derivatives. These quenched melts were found as interstitial glass inside the veins, which encloses magmatic sulfides as globules and hydrothermal ones as vug coatings, and displays relatively low S contents (down to ~200 ppm S) consistent with sulfide-saturated conditions at $-1\leq\Delta\log fO_2$[FMQ]≤ 0 (Figure 1A). Based on the observed oxidation of Fe^{2+} to Fe^{3+} in spinel from the host harzburgites, we concluded that the range in S contents in the vein MI and interstitial glass was consistent with the apparently variable fO_2 conditions. These variations resulted from a redox exchange between S^{6+} in the original melt (MI data) and Fe^{2+} in the host mantle minerals through melt–rock reactions, thereby contributing to sulfide saturation with progressive cooling (interstitial glass data; Figure 1B). Overall, these results imply that the parental LCB melts of the veins were originally undersaturated in sulfide and that they have the potential to precipitate up to 85% of their S contents as sulfides during orthopyroxenite formation in the lithosphere.

Materials and methods

Electron-probe micro-analysis

The concentrations of major base metals in sulfide minerals were determined in polished, thick (~120 μm) sections by wavelength-dispersive spectroscopy (WDS),

electron-probe micro-analysis (EPMA) on a CAMECA SX100 instrument at the Research School of Earth Sciences of The Australian National University (ANU, Australia). Analyses were performed at an accelerating voltage of 15 kV and a sample current of 20 nA. Counting times were 5–15 s on background and 10 s (Si, S, and Cu), 30 s (Fe, Co, and Ni), and 60 s (As) on the peak. Matrix effects were corrected using Phi (r) z modeling available on Peak Sight© software from CAMECA™. Errors on the measured concentrations were calculated as 3σ relative standard deviations (RSD), which typically give <4% for S, <2% for Fe, <7% for Co, <0.8% for Ni, and 0.5–20% for Cu and As. A set of standards (quartz, barite, troilite, metallic Co, metallic Ni, and metallic Cu) were analyzed as unknowns during each analytical session to estimate precision and drift, which was negligible. Major element maps were collected with the same instrument as for spot analyses but were performed at an accelerating voltage of 15 kV and an increased sample current of 40 nA. Some of the maps were collected using a Bruker energy-dispersive spectrometer coupled to the SX100 instrument.

Scanning electron microscopy

Back-scattered electron (BSE) images and semi-quantitative phase analyses at high spatial resolution were acquired using a Tescan Mira II LMU field-emission scanning electron microscope (SEM) at the University of Lausanne (UNIL, Switzerland). *In situ* analyses were performed on this instrument by energy-dispersive spectrometry (EDS) using a Penta-FET 3x X-ray detector. BSE images were acquired at a working (sample) distance of 9 mm, an accelerating voltage of 20 kV, and a sample current of ~0.5 nA, allowing a spatial resolution (spot size) of ~5 nm. EDS analyses were performed at a working distance of 20–23 mm and an increased sample current of 0.9–1.3 nA to maximize count rates, leading to a spatial resolution of 6–7.5 nm. Acquisition parameters included an energy step of 20 eV, a process time of 5 s to increase signal to background ratio and spectral resolution, and an acquisition time of 1 mn per analysis. Data treatment was made using the Oxford Instruments AZtec software packaging.

As observed in previous studies, EDS analyses of low O contents in Fe-bearing sulfides suffer from large uncertainties, mainly because of the overlap of the Fe *L* lines onto the O K_α peak. This effect has been quantified and typically returns "false" O concentrations of 0.89±0.09 wt% in O-free standards (Fonseca et al., 2008). Therefore, O in sulfides was not quantified in this study. Instead, the O K_α peak was used as a tracer of the nature of inclusions, the analyses of which were not possible due to compositional overlap effects induced by the host sulfide.

Laser ablation inductively coupled plasma mass spectrometry

The abundances of chalcophile and highly siderophile trace elements in sulfides were determined in thick sections by laser ablation inductively coupled plasma mass spectrometry (LA-ICPMS) at ANU. This system comprises a UV (λ=193 nm) Excimer laser (Lambda Physik CompEx 110) and an ANU-designed HelEx ablation cell coupled to an Agilent 7700x quadrupole ICPMS. Analyses were performed with a laser set at a 3 Hz pulse rate, 29.5 kV, 50 mJ, and using 28 µm beam diameters. For each laser ablation run, 25–30 s were counted on the carrier gas (background) followed by 35–40 s for signal. The NIST 610 glass standard (Sylvester and Eggins, 1997; Jochum et al., 2011; Kamenetsky et al., 2015) was used to calculate the concentrations of Co, Cu, Zn, Ag, Cd, Re, and Au, using ^{62}Ni as the internal standard. The CANMET po727 FeS standard (Fonseca et al., 2007; Kamenetsky et al., 2015) was used to calculate Ru, Rh, Pd, Os, Ir, and Pt (PGE) abundances, using ^{34}S as the internal standard. In both cases, internal standard concentrations were taken from EPMA data.

For all sulfide analyses, the isotopes used for data processing included ^{34}S, ^{59}Co, ^{61,62}Ni, ^{63,65}Cu, ^{64}Zn, ^{99,101}Ru, ^{103}Rh, ^{105,106,108}Pd, ^{107}Ag, ^{111}Cd, ^{187}Re, ^{189,192}Os, ^{193}Ir, ^{195,196}Pt, and ^{197}Au. The potential isobaric interferences produced by metal argides (^{40}Ar^{59}Co$^+$ over ^{99}Ru, ^{40}Ar^{61}Ni$^+$ over ^{101}Ru, ^{40}Ar^{63}Cu$^+$ over ^{103}Rh, and ^{40}Ar^{65}Cu$^+$ over ^{105}Pd) were monitored by calculating argide production rates during the analyses of PGE-free, metallic Co, Ni sulfide, and metallic Cu (C-430, Fisher Scientific™ Company), together with the natural samples (e.g., Guillong et al., 2011). The calculated production rates of metal argides during the analytical runs were small, with a range of 0.8–2.5×10^{-4}. Isobaric interferences were subtracted from the time-integrated signal, based on the measured Co, Ni, and Cu count rates in the sulfides and the argide production rates.

The accuracy and precision of the method were assessed by calculating 1σ RSD from replicate analyses of the NIST 610 glass standard during the runs, using ^{197}Au as the internal standard. Data were processed using an in-house Excel spreadsheet according to the method of Longerich et al. (1996).

Results

Petrographic observations

The complete dataset supporting this study is reported in Supplementary Table S1. For simplicity in text and figures, I refer to the fringes and central parts of the veins by using the terms "rims" and "cores", which are more conventionally used for single-grain characterization. Sulfides in the Type 1A orthopyroxenite veins from Kamchatka are distributed in a

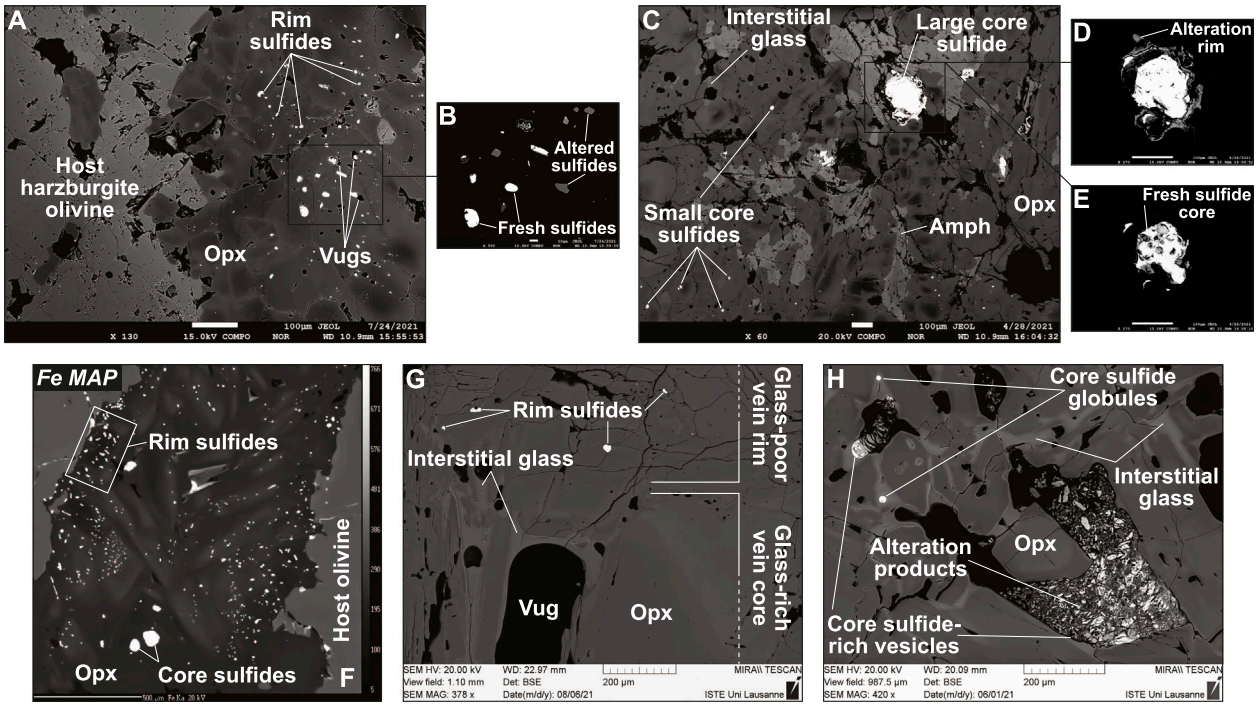

FIGURE 2
Localization and textural features of sulfides in Kamchatka and West Bismarck Type 1A veins. Data acquired using **(A–F)** EPMA and **(G,H)** SEM. BSE images of **(A,B)** vein rim sulfides and **(C–E)** vein core sulfides in the glass-bearing sample from Kamchatka (sample Av55; Bénard et al., 2022). **(F)** Fe map of the glass-free vein from Kamchatka (sample Av20; Bénard and Ionov, 2012; Bénard and Ionov, 2013; Bénard et al., 2017b). BSE images of **(G)** rim sulfides and **(H)** core sulfides in the glass-bearing vein from West Bismarck (sample 67-02E (3); Bénard et al., 2018c). Scale bar is 100 µm in **(A)** and **(C–E)**, 10 µm in **(B)** and 500 µm in **(F)**. Note the generally smaller sizes of rim sulfides, which are also more abundant than core sulfides, presumably because of the higher melt-rock reaction rates with S^{6+}-Fe^{2+} redox exchange in the former areas (see text for details). Sulfide-rich vesicles are only present in the glassy core of the West Bismarck vein. Amph, amphibole.

similar manner, whether the vein contain glass (sample Av55; Figures 2A–E) or not (sample Av20; Figure 2F). Small sulfides are abundant at vein rims (Figures 2A,B,F), whereas sparse, larger sulfides can be found in the vein cores (Figures 2C–F). A similar grain coarsening trend from vein rims to vein cores has been previously identified for opx (Bénard and Ionov, 2012; Bénard and Ionov, 2013; Bénard et al., 2022), which can also be accompanied by the presence of more abundant glassy areas toward the core. The latter glass enrichment trend is more obvious in the Type 1A orthopyroxenite vein from West Bismarck (sample 67-02E(3); Figures 2G,H), where sulfides are generally less abundant than in Kamchatka veins. While most sulfides appear as globules, which are frequently associated with small vugs or traces of glass, West Bismarck veins are characterized by the presence of sulfide-rich vesicles in glassy areas as well (Figure 2H). Alteration of sulfides is more pronounced in those vesicles, but secondary transformation of globules also occurs when they are associated with vugs (Figures 2B,D,H). EDS analysis reveals that the secondary assemblages formed from sulfides are essentially composed of Fe oxyhydroxide (FeO(OH)) with accessory magnetite (Supplementary Figures S1, S2 and Supplementary Table S1).

All sulfides in the Kamchatka veins appear as homogeneous phases from BSE images and element mapping, which also corroborate the common association of this phase with glass, even when it is included in opx (Figures 3A–G and Supplementary Figure S3). EDS characterization of the sulfides confirm their homogeneity at the sub-micron scale, even when this phase appears in opx-hosted MI (Supplementary Figures S3, S4). The only exception to this tendency is found in the Kamchatka glass-free vein, which has homogeneous rim sulfides associated with trails of minute, euhedral oxide grains but heterogeneous core sulfides with exsolutions (Figures 3H,I and Supplementary Figure S3). These exsolutions have already been identified in an earlier study of glass-free veins from Kamchatka, using three-dimensional imaging (Bénard et al., 2011). Here, EDS characterization reveals that these exsolutions are associated

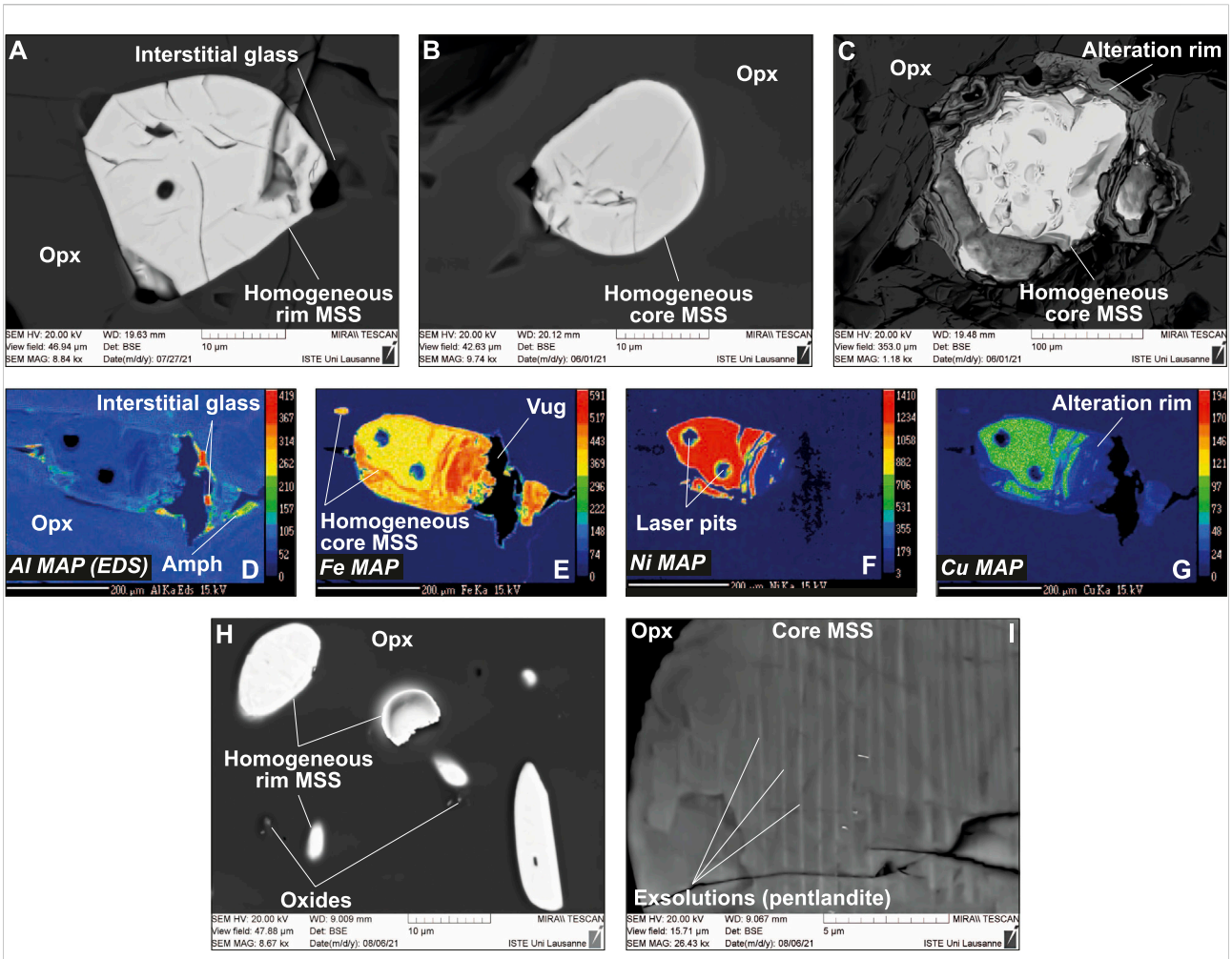

FIGURE 3
Textural features of sulfides (all MSS) in Kamchatka Type 1A veins. **(A–C)** BSE images (SEM) and **(D–G)** major element maps (EPMA) for sulfides either located at rims or cores of the glass-bearing vein (sample Av55). **(H,I)** BSE images (SEM) for sulfides either located at rims or cores of the glass-free vein (sample Av20). Scale bar is 200 µm in **(D–G)**, whereas the elements mapped are indicated in the bottom left corners of the images. Small oxides appear associated with rim sulfides in the glass-free vein from Kamchatka in **(H)**. Note the homogeneity of MSS in all Kamchatka samples, except for pentlandite exsolutions in core sulfides from the glass-free sample in **(I)** (see Bénard et al., 2011 for an earlier identification of this feature).

with higher Ni contents, which most likely trace pentlandite (Supplementary Figure S3).

Sulfides in the West Bismarck vein display more complex textural features and phase assemblages than those from Kamchatka. Both inclusion-bearing and homogeneous sulfides are found at vein rims (Figures 4A,B), while heterogeneous globules (i.e., unmixed into different sulfide phases) are found at veins rims and in the glassy areas of the vein core (Figures 4C–F). EDS characterization of the heterogeneous globules indicate that they are mostly composed of Fe- and Ni-rich phases in variable abundances, together with a minor Cu-rich phase (Figures 4C–F and Supplementary Figure S5). Element mapping confirms the relative abundances of the different phases in the heterogeneous globules (Figures 4G–J and Supplementary Figure S6). EDS characterization of inclusion-bearing rim sulfides allow identifying these inclusions as oxides (Figures 5A–D and Supplementary Figure S7), which are also found in clear association with the Cu-rich parts of heterogeneous globules (Figures 5E–G). Trails of minute, oxide grains were also found, albeit very rarely, in the interstitial glass surrounding some of the West Bismarck vein sulfides (Supplementary Figure S8).

Alloys and native metals were found in different parts of both Kamchatka and West Bismarck veins. Pt alloys were identified on the surface of nearly all the different types of sulfides described above, which include the homogeneous (Figures 6A–D and Supplementary Figure S9) and heterogeneous (Figures 6E–H) globules, as well as the sulfide-rich vesicles (Supplementary

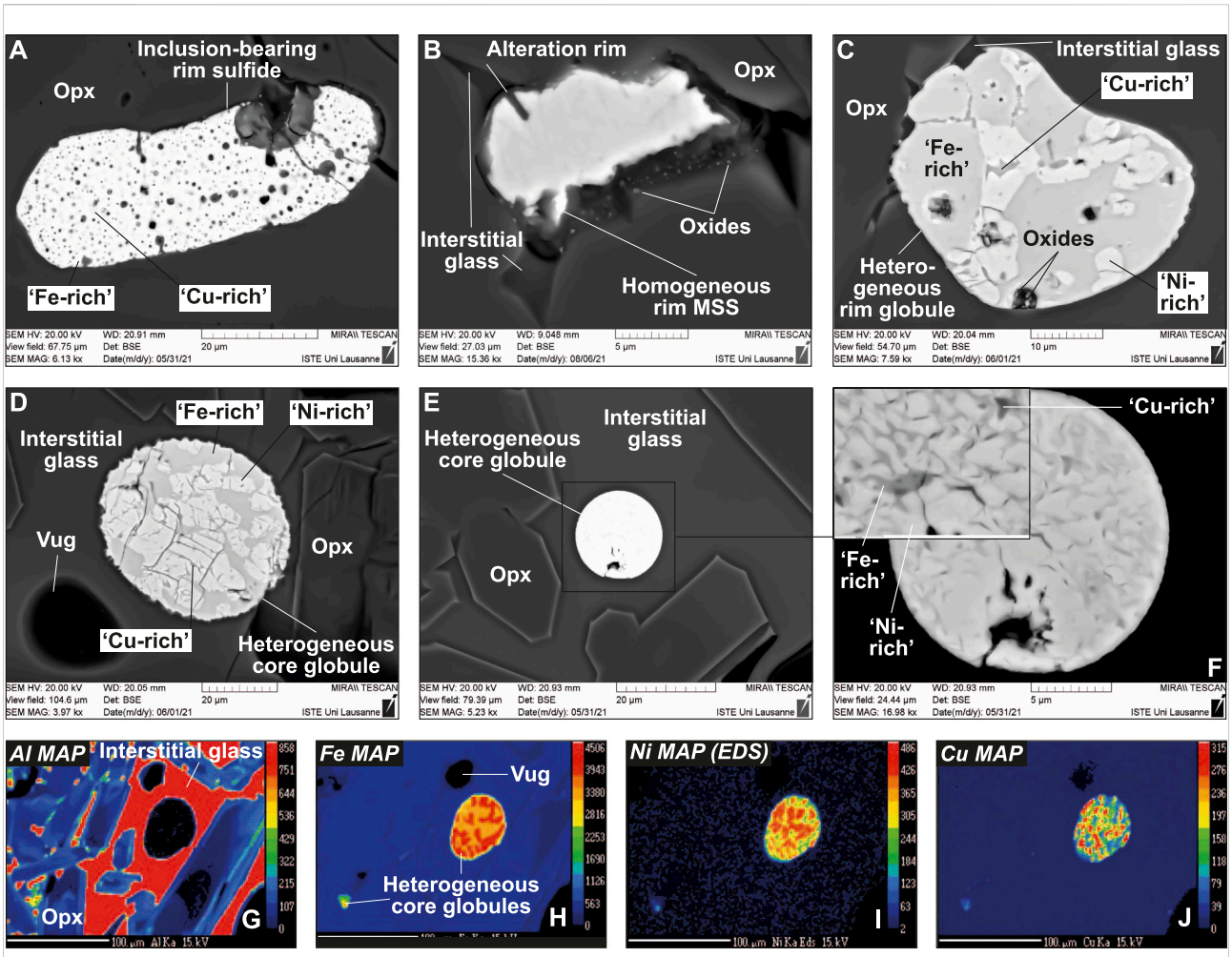

FIGURE 4
Textural features of sulfides (all MSS or "xSS") in the glass-bearing, Type 1A vein from West Bismarck. **(A–F)** BSE images (SEM) and **(G–J)** major element maps (EPMA) for vein core sulfides. Scale bar is 100 μm in **(G–J)**, whereas the elements mapped are indicated in the top left corners of the images. Note the homogeneity of some rim MSS, whereas all core globules are heterogeneous.

Figure S10). Some of these Pt alloys are located near the sulfides and can contain Rh at levels detectable by EDS (Supplementary Figure S10). Metallic Fe was found in curvilinear vugs, which are located in glassy areas and coated with altered sulfides (now found as Fe oxyhydroxide) and Cl-rich amphibole (Supplementary Figures S11, S12; Bénard et al., 2022). Wüstite was also clearly identified in those vugs, among different types of alloys, which are also abundantly found in these areas (Supplementary Figure S13).

Major base metals

All Kamchatka vein globules are monosulfide solid solutions (MSS; $(Fe, Ni)_{1-x}S$), which typically form at ca. 1,000–1,100°C (Figure 7A; Craig and Kullerud, 1969; Kullerud et al., 1969). In the Kamchatka glass-free veins, core MSS is dramatically enriched in Ni in comparison with rim MSS (Figure 7A). Bulk sulfide analysis of West Bismarck vein globules by EPMA show that these phases range in composition from high-T MSS (homogeneous globules) to Cu-enriched sulfides (heterogeneous globules), which presumably formed at least down to 900°C (Figure 7A; Craig and Kullerud, 1969; Kullerud et al., 1969).

Further EDS analyses reveal that the heterogeneous globules are made of two MSS phases (one being enriched in Fe and the other in Ni), in addition to the Cu-rich phase (Supplementary Table S1). A comparison with the sulfide crystallization experiments of Fleet et al. (1993) and Fleet and Pan (1994) shows that the compositional range of this Cu-rich phase is similar to that of a (Fe, Cu, Ni)S ternary solid solution ranging between MSS and intermediate solid

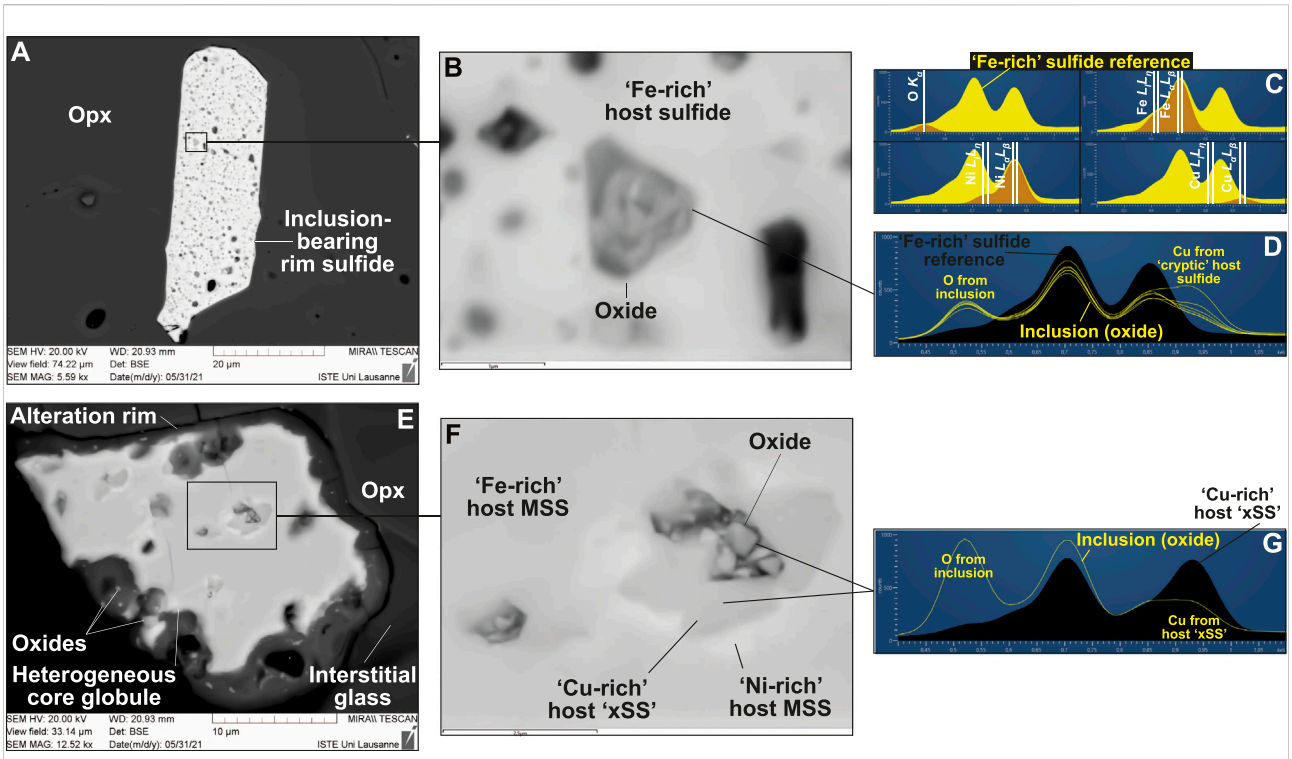

FIGURE 5
Oxide inclusions in sulfides from the glass-bearing, Type 1A vein from West Bismarck (SEM). BSE images of **(A,B)** a rim sulfide and **(E,F)** a core sulfide. The EDS spectra for those oxides and their host sulfides are respectively shown in **(D)** and **(G)**, with peak identification in **(C)**. Note that oxide inclusions are associated with "Cu-rich" sulfide ("xSS"), either identified using EDS spectra only in **(D)** ("cryptic") or also clearly visible in BSE images in **(E,F)**. Non-included oxides are localized at sulfide rims in **(E)**.

solution (ISS; (Cu, Fe)S_{1-x}) (Figure 7A and Supplementary Table S1). This phase forms below 850°C and was named "xSS" by Fleet et al. (1993) (Figure 7A). By comparing EDS spectra, this Cu-rich phase is also identified as a component of inclusion-bearing sulfides, where it appears to be preferentially located around the oxide inclusions (Figures 5C,D,G, Supplementary Figure S7 and Supplementary Table S1).

The bulk compositions of some heterogeneous globules were calculated using EDS analyses of their constitutive, MSS and xSS, as well as phase proportions derived from BSE image processing (i.e., pixel counting with the software PHOTOSHOP from Adobe® Company; Supplementary Table S1). Combining these calculations with all other phase analyses, the major base metal compositional range of Kamchatka and West Bismarck vein sulfides describes sharp Ni and Cu enrichment trends, consistent with a sulfur depletion relative to the sum of metals in their compositions (i.e., increasing atomic ∑metal/S; Figures 7B,C). Notably, sulfide compositions are consistent with decreasing temperatures of crystallization from vein rims to vein cores, and from the Kamchatka setting to the West Bismarck one (Figures 7A–C).

Chalcophile and highly siderophile trace elements

Some Kamchatka MSS were large enough to perform replicate LA-ICPMS analyses and confirm their homogeneity (Figures 3D–G and Supplementary Figure S3), but most sulfides were relatively small so that the signal integrated for quantification was sometimes as short as ca. 20–30 s. However, the consistency of the data supports the fact that short integration times had an insignificant effect on data quality, likely because of very high signal/background ratios (Figure 8 and Figure 9). Kamchatka vein sulfides with relatively flat LA-ICPMS signals generally have similar, chondrite-normalized patterns (Figures 8A–C; Palme and O'Neill, 2014). Most of these patterns are characterized by a depletion of IPGE relative to PPGE, with a pronounced Ir negative anomaly relative to Os and Ru (Figure 8A). However, this Ir depletion is apparently absent from the rim sulfides of the glass-free veins from Kamchatka, which are inferred to be those formed at the highest temperatures in this study (Figure 7A and Figure 8A).

West Bismarck vein sulfides with relatively flat LA-ICPMS signals generally have chondrite-normalized

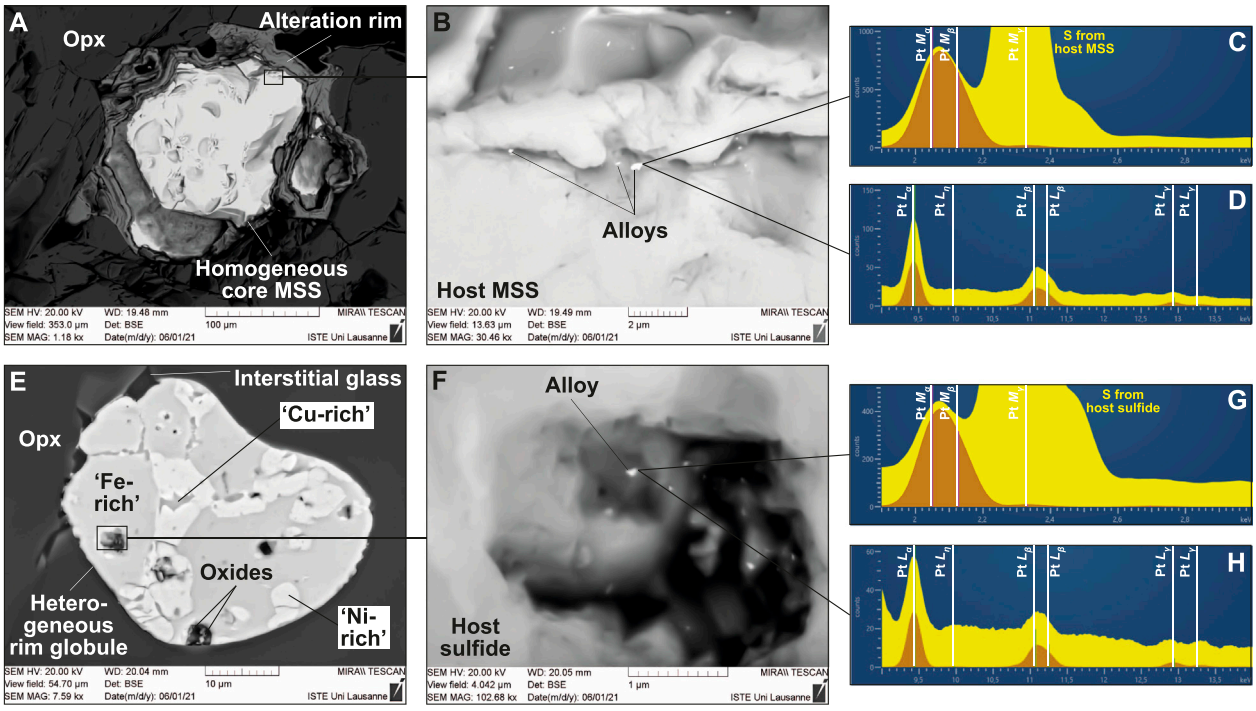

FIGURE 6
Pt alloys located on sulfides from the glass-bearing, Type 1A veins from Kamchatka and West Bismarck (SEM). BSE images of **(A,B)** a core sulfide in the Kamchatka vein and **(E,F)** a rim sulfide in the West Bismarck vein. The EDS spectra for those Pt alloys and their host sulfides are respectively shown in **(C,D)** and **(G,H)** with peak identification. Note that Pt alloys can be found in association with **(A)** homogeneous sulfides and **(E)** heterogeneous globules, respectively, ranging from "Fe-rich" (MSS) to "Cu-rich" ("xSS") compositions.

patterns alike those from Kamchatka, though they differ in a few key points (Figures 8D,E). All West Bismarck vein sulfides are characterized by much lower Pd, with chondrite-normalized Pt/Pd systematically ranging above unity (Figure 8D). Some of the heterogeneous globules were analyzed using LA-ICPMS, which reveals that they have PGE and Re abundances like homogeneous MSS (Figure 8D). However, heterogeneous globules are characterized by higher Au, Ag, and Cu contents (Figure 8D). In the case of Cu, this observation is consistent with the major base metal dataset (Figures 7A,C and Supplementary Table S1).

Some of the sulfides analyzed by LA-ICPMS display compositional evidence for the contributions of Pt alloys, as revealed by positive spikes in the ablation signals and chondrite-normalized patterns ("nugget effect": Figures 9A–D). In both Kamchatka and West Bismarck sulfides, Pt positive spikes are commonly coupled with higher levels of Rh and Au, and to varying extents, Os and Ir (Figures 9A,C). Some of the largest positive spikes in the ablation signals were used to derive semi-quantitative estimates of the Pt alloy compositions (i.e., on an Fe-free basis), which give 90–93 wt% Pt, 0.1–6 wt% Rh, 2–5 wt% Au, ~1 wt % Os, and traces of Ir and Ru (Supplementary Table S1).

Discussion

Sulfide liquid line of descent and P-T-fO_2-fS_2 constraints

A wide compositional range in major base metals is preserved on a small scale in Kamchatka and West Bismarck vein sulfides (Figures 7A–C). Since all the sulfides are armored in orthopyroxenite veins, which were previously demonstrated to be melt channels (Bénard and Ionov, 2012; Bénard and Ionov, 2013; Bénard et al., 2018c; Bénard et al., 2022), these phases must have formed from a common, original sulfide liquid genetically linked to LCB. Below, I discuss the compositional relationships between the different vein sulfides to track the evolution trends of their parental liquids. I also use thermodynamic calculations to constrain the physicochemical conditions of their crystallization.

One of the key differences between the Kamchatka and the West Bismarck setting concerns the equilibration temperatures of the spinel harzburgites hosting the orthopyroxenite veins, which are significantly higher in the former (900–1,000°C; Bénard and Ionov, 2012; Bénard and Ionov, 2013; Bénard et al., 2022) than in the latter (750–800°C; Bénard et al., 2018c). This temperature difference is related to varying

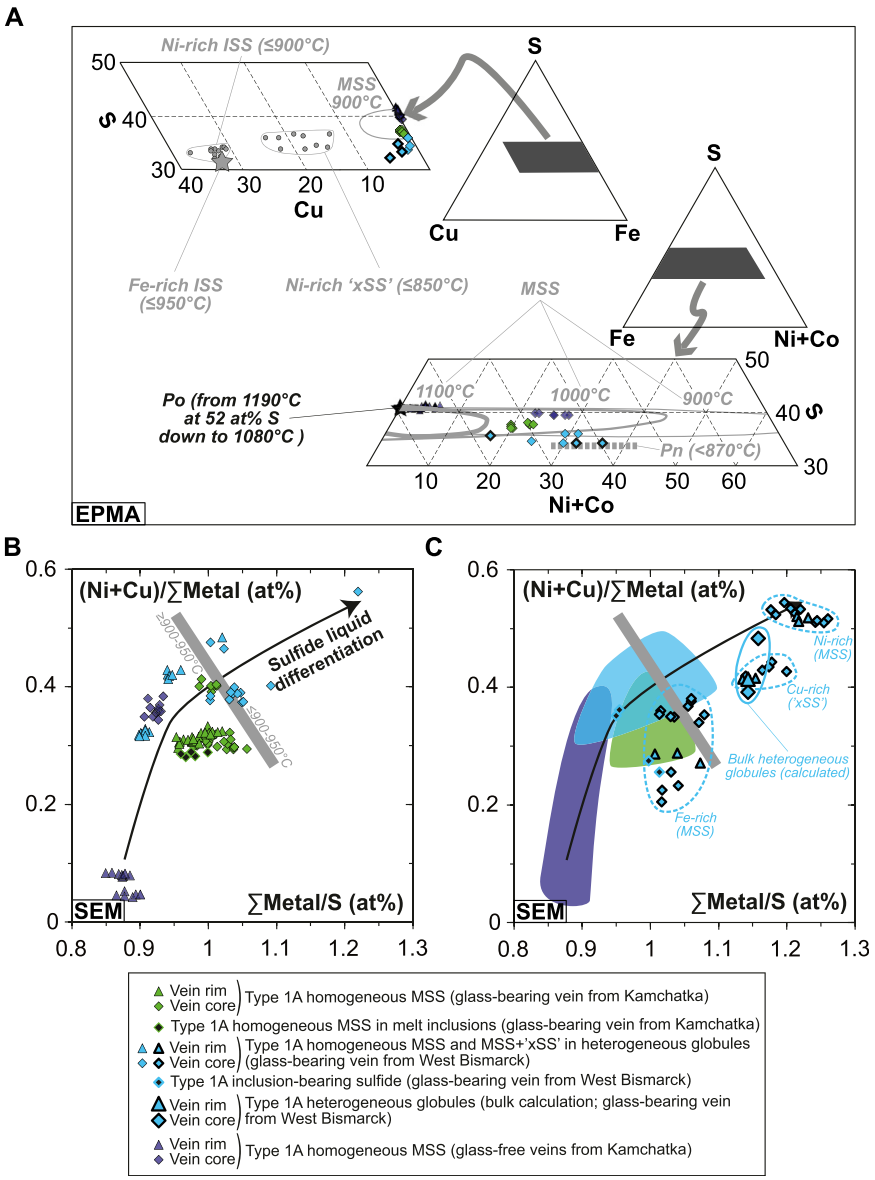

FIGURE 7
Major element abundances in the Kamchatka and West Bismarck vein sulfides. **(A)** Sulfide compositions (EPMA) plotted in triangular projections of the Fe(±Ni, Co)-Cu-S system (all in wt%). The heterogeneous globules from West Bismarck are indicated using symbols with a bold black contour. **(B,C)** (Ni+Cu)/∑Metal plotted against ∑Metal/S for **(B)** homogeneous and **(C)** heterogeneous globules (SEM; all in at%). The homogeneous sulfide data are shown with fields in **(C)**. Literature data for experimental sulfide phase relations (with stability field temperatures) and compositions in **(A)** include MSS (solid gray lines; Craig and Kullerud, 1969; Kullerud et al., 1969), pyrrhotite (Po, black star; Fleet, 2006; Mungall, 2007), pentlandite (Pn, dotted gray line; Lorand, 1989; Fleet, 2006; Mungall, 2007), Ni-rich "xSS" and ISS (gray dots; Fleet et al., 1993; Fleet and Pan, 1994), and Fe-rich ISS (gray star; Ballhaus et al., 2001). As elsewhere, black symbols stand for literature data in the Fe-S(-O) system, whereas gray symbols stand for literature data in the Fe(±Ni, Co)-S(-O) system.

crustal thicknesses aong the two settings (Bénard et al., 2018a); it has further been confirmed in studies of vein-free harzburgite samples from both Kamchatka (900–1,000°C; Ionov, 2010) and West Bismarck (650–700°C; Bénard et al., 2017a). This translates into undercooling degrees (ΔT) of, respectively, 100–200°C and 300–450°C for the glass-forming, high-Mg# andesite melt when using mineral-glass thermometry data (~1,100°C; Bénard et al., 2018c, 2022; Figure 10A). Since the equilibration conditions of the ambient sub-arc mantle virtually correspond to the lower-end temperatures for the LCB melt evolution path in the veins (e.g., andesitic glass in Kamchatka versus andesitic and dacitic glasses in West Bismarck; Figure 1A), it is also likely that these varying equilibration conditions have had contrasting effects on the sulfide liquid line of descent.

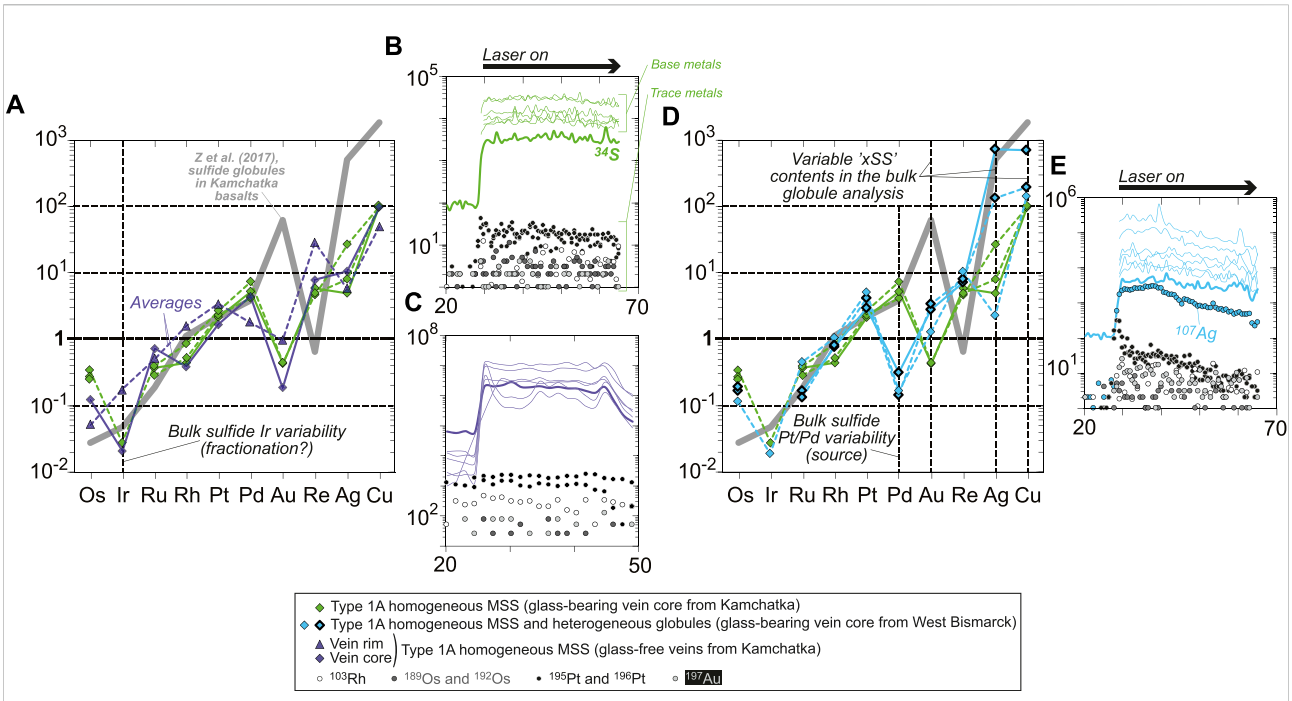

FIGURE 8
Chondrite-normalized (Palme and O'Neill, 2014) abundances of chalcophile and highly siderophile trace elements in sulfides from **(A)** Kamchatka (core and rim sulfides) and **(D)** West Bismarck (core sulfides only) Type 1A veins. The heterogeneous globules from West Bismarck are indicated using symbols with a bold black contour. Representative LA-ICPMS signals for **(B,C)** Kamchatka and **(E)** West Bismarck sulfides (corresponding to solid patterns in chondrite-normalized plots) are also shown. None of these sulfides display significant spikes in their laser ablation signals. Note the changing Ir depletion degrees in **(A)**, and the variable Pt/Pd and Au, Ag, and Cu contents in **(D)**. The latter two features can be used to characterize West Bismarck sulfides, which have systematically high Pt/Pd and can be enriched in Au, Ag, and Cu (heterogeneous globules) relative to Kamchatka sulfides. Literature data included for comparison in **(A)** and **(D)** are chondrite-normalized patterns of "nugget-free" sulfide globules from Tolbachik volcano lavas (high-Mg basalts) in Kamchatka (solid gray patterns; Zelenski et al., 2017).

The undercooling degree of Kamchatka vein glass brackets the tight temperature interval spanned by the liquidus–solidus field for MSS in the Fe-Ni-Cu-S system (Figure 10A; Zhang and Hirschmann, 2016), whereas that of West Bismarck vein glass extends well below the solidus. The xSS and MSS phases in the heterogeneous globules from West Bismarck appear in chemical equilibrium with respect to their metal contents, when compared to experimental data in the Fe-Ni-Cu-S system (Figure 10B; Fleet et al., 1993; Fleet and Pan, 1994). Therefore, the calculated, bulk compositions of these heterogeneous globules most likely represent a precursor sulfide phase, which subsequently unmixed because of the lower temperature conditions characterizing the West Bismarck sub-arc mantle (Fleet, 2006). Therefore, it is unsurprising that these heterogeneous globules, as well their constitutive xSS and oxides, were not found in Kamchatka veins (Figure 3).

Collectively taken, sulfide compositions describe Ni and Cu enrichment trends at decreasing sulfur contents (Figures 10C,D). These trends are consistent with sharp increases in the atomic (Ni+Cu)/∑metal and ∑metal/S from the Fe-rich MSS at the rims of Kamchatka glass-free veins to the West Bismarck heterogeneous globules (Figures 7B,C). These two sulfide species represent the end-members formed at the highest and lowest temperatures, respectively (Figure 7A). First, increasing ∑metal/S in MSS is expected to depress the solidus of this phase further than what is shown in Figure 10A (Ballhaus et al., 2001; Ballhaus et al., 2006; Zhang and Hirschmann, 2016). Second, increasing (Ni+Cu)/∑metal and ∑metal/S in MSS provide evidence for the nature of the sulfide liquid line of descent (e.g., Ballhaus et al., 2001; Mungall et al., 2005).

The Ni and Cu enrichments in homogeneous MSS result of progressive cooling (presumably because of increasing defect concentrations in the solid solution), which is consistent with phase relations in the Fe-Ni-S system (Figure 7A; Kullerud et al., 1969; Ballhaus et al., 2001). For the ∑metal/S in MSS to increase as in West Bismarck veins (i.e., up to ~1.15, whereas all sulfides in the glass-free Kamchatka vein range at 0.9±0.5; Figures 7B,C), temperature must have dropped well below 900°C. Furthermore, the greatest increases in (Ni+Cu)/∑metal in MSS are experimentally observed for parental sulfide liquids, which originally have the lowest ∑metal/S ranging from ~0.9 to ~1 (Ballhaus et al., 2001). Finally, these low-∑metal/S sulfide liquids

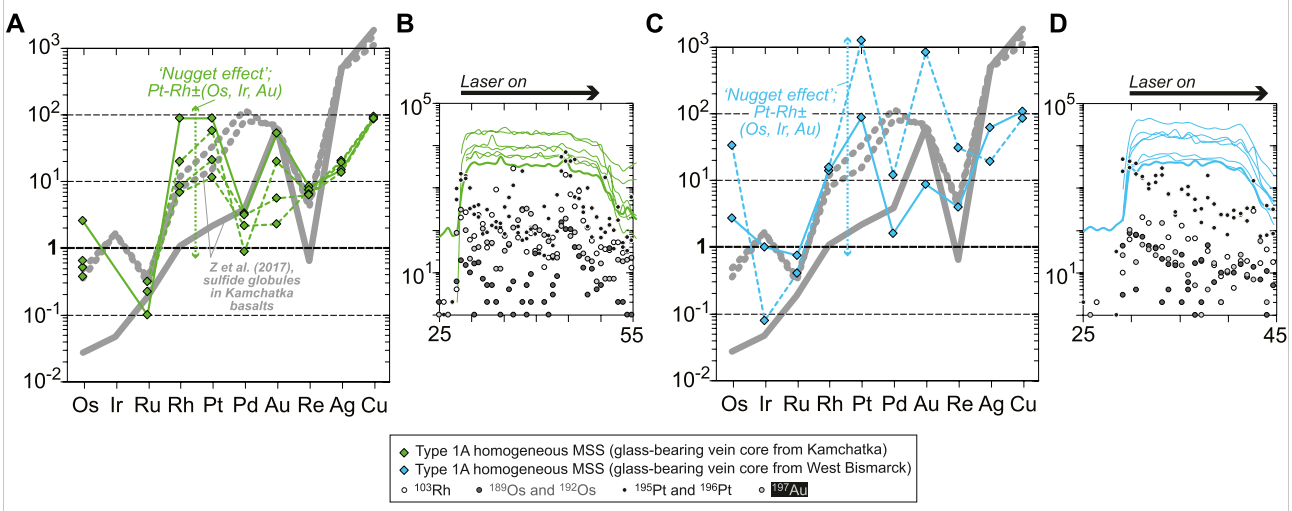

FIGURE 9
Chondrite-normalized (Palme and O'Neill, 2014) abundances of chalcophile and highly siderophile trace elements in core sulfides from **(A)** Kamchatka and **(D)** West Bismarck Type 1A veins. Representative laser ablation signals for **(B)** Kamchatka and **(D)** West Bismarck sulfides (corresponding to solid patterns in chondrite-normalized plots) are also shown. All these sulfides display significant spikes in their laser ablation signals, resulting from the presence of Pt alloys ("nugget effect"). Note that Pt spikes are combined with those of Rh, and to varying extents, Os, Ir and Au in **(A)** and **(C)**. Literature data included for comparison in **(A)** and **(C)** are chondrite-normalized patterns of "nugget-free" (solid gray patterns) and "nugget-bearing" (dotted gray patterns) sulfide globules from Tolbachik volcano lavas (high-Mg basalts) in Kamchatka (Zelenski et al., 2017).

will likely solidify in the stability field of ISS; that is, they will not produce eutectic, Cu-rich phase assemblages formed at even lower temperatures (Ballhaus et al., 2001).

From the considerations above and the low ∑metal/S of Fe-rich MSS formed at the highest temperatures in this study (0.85–0.9; Figures 7A,B), it can be implied that the compositional evolution of LCB vein sulfides reflects parental liquids with originally low ∑metal/S of ~0.9. Such sulfide liquid is often referred to as "oxidized" since it is mainly O that substitutes for S (see for instance the experiments in the MS-12 system from Ballhaus et al., 2001). It is thus likely that such sulfide liquid will also fractionate some oxides, reflecting fO_2 conditions approaching the FMQ buffer during crystallization (e.g., Naldrett, 1969). Some of these oxides appear to have formed at an early stage, as observed near the high-T, Fe-rich MSS (Figure 3H). Oxides also occur in association with Ni-rich MSS and Cu-rich xSS, suggesting that they formed all along the sulfide liquid of descent with decreasing temperature (Figures 4B, 5F and Supplementary Figures S7, S8). These features are consistent with those of Ni-Cu-PGE ore samples, with magnetite occurring as a cotectic phase from MSS to ISS formation (Duran et al., 2020); although the oxides near LCB sulfides were generally too small to be analyzed, these are most likely magnetite. Magmatic chromite grains were also observed in all the veins in this study, but no in clear association with sulfides (e.g., Bénard et al., 2022), as it should be when crystallization occurs along a sulfide-spinel cotectic or during O loss from a sulfide liquid (Fonseca et al., 2008). The elevated Cr/(Cr+Al)≥0.75 of vein chromite also suggest that they rather formed at higher temperatures than MSS, most likely by direct precipitation from the silicate melt fraction in LCB magmas (Bénard and Ionov, 2012; Bénard and Ionov, 2013; Bénard et al., 2018c; Bénard et al., 2022).

Further constraints on the fO_2 and fS_2 conditions prevailing throughout the LCB sulfide liquid line of descent require independent thermodynamic calculations. All the glass-bearing veins in this study contain traces of magmatic olivine, which typically has higher Mg# than in the host spinel harzburgite (0.91–0.93; Bénard et al., 2018c; Bénard et al., 2022). The presence of this phase indicates that the thermodynamic activity of the fayalitic component was fixed during the formation of the orthopyroxenite veins, allowing the use of the olivine-opx+MSS equilibrium for fO_2 and fS_2 calculations. Using Equations 41 and 46 from the calibration of Eggler and Lorand (1993) for this equilibrium, I calculate fS_2 conditions for the LCB vein crystallization, assuming 1) $-1 \leq \Delta \log fO_2[\mathrm{FMQ}] \leq 0$ inferred from the sulfur contents at sulfide/sulfate saturation (SCSS) measured in the S-poor, vein interstitial glass (Figures 1A,B; Smythe et al., 2017); and 2) an Mg# varying from 0.84 to 0.93 in olivine, which matches the full compositional range of the coexisting vein opx (Bénard et al., 2018c; Bénard et al., 2022). Results show that at 0.5 GPa, which is likely the minimum pressure for the formation of the veins (Figure 1A; Bénard et al., 2018c; Bénard et al., 2022), the

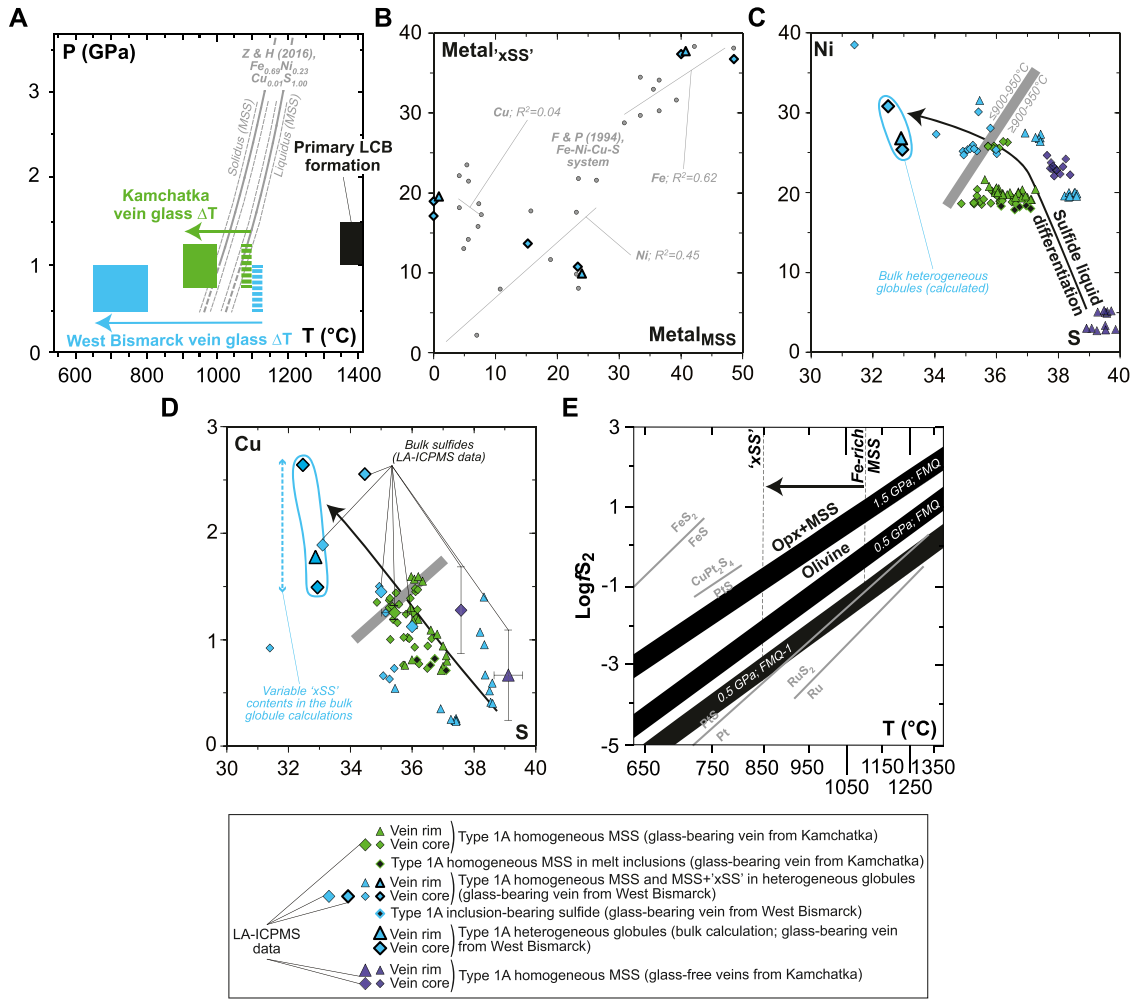

FIGURE 10
Constraints on sulfide formation and sulfide liquid fractionation for Kamchatka and West Bismarck Type 1A veins (SEM). **(A)** Plot of pressure against temperature showing the variable undercooling degrees (ΔT) experienced by the glass-forming melt in veins from Kamchatka (green fields) and West Bismarck (blue fields). These are compared with the experimental liquidus and solidus of MSS in the Fe-Ni-Cu-S system (gray lines; Zhang and Hirschmann, 2016). The inferred P-T conditions of primary melts formed from spinel harzburgite sources, as modeled by Bénard et al. (2018c) (black field) are also shown. **(B)** Relationships between metal abundances (Fe, Ni, and Cu) in "xSS" and MSS from heterogeneous globules in the West Bismarck vein (all in wt%). These data are compared with the experimental results of Fleet and Pan (1994) in the Fe-Ni-Cu-S system (gray dots). **(C)** Ni and **(D)** Cu plotted against S for Kamchatka and West Bismarck vein sulfides (all in wt%). The heterogeneous globules from West Bismarck are indicated using symbols with a bold black contour. **(E)** Plot of fS_2 (in log units) against temperature showing a range of vein sulfide formation conditions (black fields), calculated using the olivine-opx+MSS equilibrium for variable P-T-fO_2 values following Eggler and Lorand (1993) (see text for details). Also shown in gray are fS_2-T relationships for the univariant Ru-RuS_2 and Pt-PtS curves (Barin, 1995), the stability field of malanite ($CuPt_2S_4$; Peregoedova and Ohnenstetter, 2002), and the univariant FeS-FeS_2 curve (Vaughan and Craig, 1978). Note that the lower-end, P-fO_2 conditions inferred from SCSS data in Figures 1A,B (0.5 GPa; FMQ-1), together with the temperature range for Fe-rich MSS to xSS crystallization (ca. 850–1,100°C; black arrow), place fS_2-T conditions for the formation of vein sulfides close to the Pt-PtS univariant curve.

crystallization sequence from Fe-rich MSS (ca. 1,050–1,100°C) to xSS (≤850°C) will occur at relatively low fS_2 ranging from −3.5 to −1 bars in log units (Figure 10E). When compared with a series of univariant reaction curves, these fS_2 values place the vein sulfide crystallization conditions close to the Pt-PtS buffer (Figure 10E; Barin, 1995). The latter point is consistent with the widespread distribution of Pt alloys near all types of sulfides in the glass-bearing veins from both Kamchatka and West Bismarck (Figure 6 and Supplementary Figures S1, S9, S10).

From the inferred, low ∑metal/S of the parental sulfide liquids in LCB, it appears that heterogeneous globules made of MSS and xSS in West Bismarck veins are aggregates of different crystallization products from these liquids. Therefore, none of the phases analyzed in this study can be considered as a

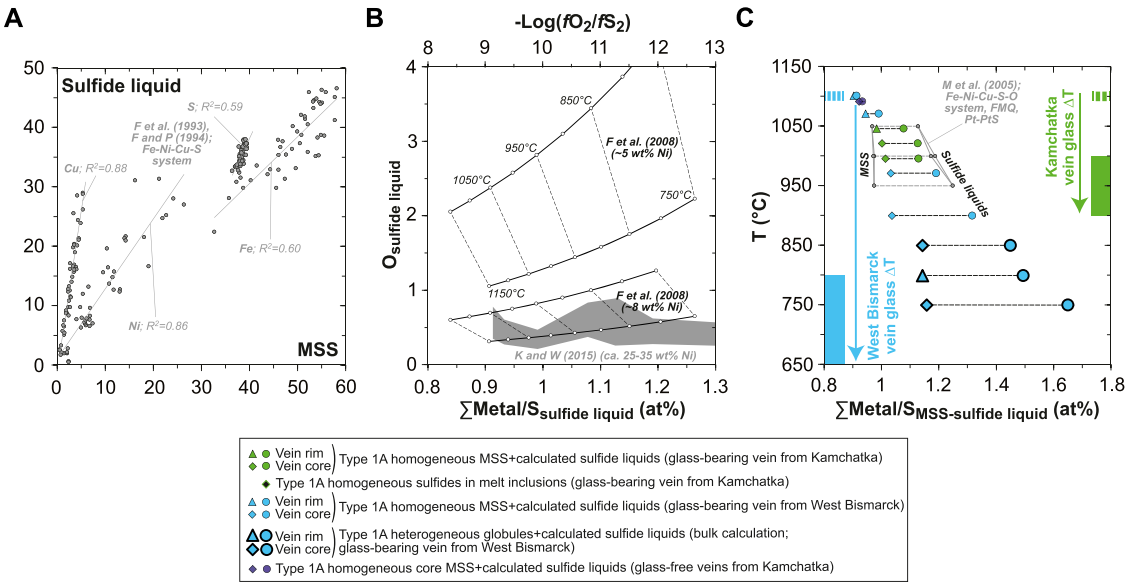

FIGURE 11
Estimates of the compositions of the parental sulfide liquids in Kamchatka and West Bismarck Type 1A veins (SEM). **(A)** Relationships between metal (Fe, Ni and Cu) and S abundances in sulfide liquid and MSS for the experimental results of Fleet and Pan (1994) in the Fe-Ni-Cu-S system (gray dots; all in wt%). **(B)** Relationships between O abundances (wt%) in sulfide liquids and their ∑Metal/S (at%) or $-\log(fO_2/fS_2)$. Results using the solubility model of O in sulfide liquids from Fonseca et al. (2008) are plotted against $-\log(fO_2/fS_2)$ (black lines with white dots), whereas those using the solubility model of O in sulfide liquids from Kiseeva and Wood (2015) are plotted against ∑Metal/S (gray field). Both models give consistent O solubilities (ca. 0.5 to 2 wt%) as Ni contents increase from ~5 to ~8 wt% and above in sulfide liquids, which is the case for those derived from LCB (see text for details). **(C)** Relationships between temperature and ∑Metal/S (at%) for MSS (diamonds) and their parental sulfide liquid estimates (dots) in Kamchatka and West Bismarck veins. Also shown are the variable undercooling degrees (ΔT) experienced by the glass-forming melt in veins from Kamchatka (green fields) and West Bismarck (blue fields). Data are compared with experimental MSS and sulfide liquids from Mungall et al. (2005) in the Fe-Ni-Cu-S-O system (gray dots).

quenched sulfide liquid, the composition of which must be derived by calculations using experimental data.

Estimates of the compositions of sulfide liquids in magmas derived from spinel harzburgite sources

In order to estimate the compositions of the parental liquids of vein sulfides, I use two main calculations combined in an iterative approach. First, I estimate the major base metal concentrations in the sulfide liquid in equilibrium with all sulfides analyzed in this study; that is, over temperatures ranging from ~1,100°C down to ~900°C using the compositions of homogeneous, Ni-rich MSS, and at ca. 750–850°C using the calculated compositions of bulk heterogeneous globules (i.e., MSS+xSS; Figure 7A). Thus, I hypothesize that these bulk heterogeneous globules constitute a cumulate mixture of different sulfide phases. For this first step, I use the metal partitioning data between MSS and sulfide liquid from the experiments of Fleet et al. (1993) and Fleet and Pan (1994) in the Fe-Ni-Cu-S system (Figure 11A). Second, I estimate O solubility in the calculated sulfide liquids using two relationships: 1) as a function of sulfide liquid composition, temperature, fO_2 and fS_2 using Equation 7 in Fonseca et al. (2008); and 2) as a function of silicate melt and sulfide liquid compositions using Equation 6 in Kiseeva and Wood (2015). In the first case, fO_2 and fS_2 are set using Equations 41 and 46 in Eggler and Lorand (1993), for $-1 \leq \Delta \log fO_2[FMQ] \leq 0$ and a Mg# varying from 0.84 to 0.93 in olivine. In the second case, the lower- and upper-bound FeO_t contents of the silicate melt (respectively ~4 and ~9 wt%) are derived from the analyses of the high-Mg# andesite vein glass (Bénard et al., 2018c; Bénard et al., 2022).

Results show that O solubility in the calculated sulfide liquids are predicted in a consistent way by both the parameterizations of Fonseca et al. (2008) and Kiseeva and Wood (2015) (Figure 11B). Because of the well-known effect of the presence of Ni on lowering O solubility in sulfide liquids (see Fonseca et al., 2008 and references therein), the calculated concentrations of the latter element drop below ~2 wt% once Ni exceeds ~5 wt%, which is the case for LCB sulfide liquids (Figure 11B). The upper O concentrations predicted for sulfide liquids formed in equilibrium with Ni-rich MSS in LCB generally do not exceed ~1 wt% when inferred from the parameterization of Kiseeva and

Wood (2015), which I use for the calculations reported here (Figure 11B and Supplementary Table S1). The low O contents calculated for the sulfide liquids formed from LCB are consistent with the limited amounts and small sizes of primary oxides in clear association with sulfides in the veins (Figures 3H, 4B, 5F and Supplementary Figures S7, S8).

As their daughter MSS, the estimated sulfide liquids are particularly rich in Ni (from ~25 to ~35 wt%; Supplementary Table S1), while they experience a pronounced increase in their ∑metal/S with decreasing temperature (≥1.2 at ≤1,000°C; Figure 11C and Supplementary Table S1). The latter trend was not reproduced in differentiation experiments of sulfide liquids with initially low ∑metal/S (0.9–1), as this parameter was only reaching ca. 1.1–1.2 at 950°C with progressive MSS fractionation (Ballhaus et al., 2001). It should be noted, however, that the experimental design in Ballhaus et al. (2001) included: 1) original charge compositions calculated to simulate equilibrium with a tholeiitic basalt (i.e., fertile mantle sources); 2) fO_2 left unbuffered during the experimental runs, though it was probably kept to a minimum, and fS_2 intrinsically defined by the compositions of sulfides; and 3) no run temperatures below 880°C. In experiments where fO_2 and fS_2 were respectively constrained at the FMQ and Pt-PtS buffers (Mungall et al., 2005), elevated ∑metal/S like those calculated in this study were encountered (Figure 11C). In this Fe-Ni-Cu-S-O system, Ni enrichment can further occur in sulfide liquids (i.e., this element is even more incompatible), when fS_2 conditions range from the Pt-PtS buffer to even lower partial pressures (Craig and Kullerud, 1969; Ebel and Naldrett, 1996; Mungall et al., 2005).

The estimated sulfide liquid line of descent in LCB is therefore consistent with the evolution of an originally Ni-rich and Cu-poor sulfide liquid at fO_2 and fS_2 conditions, which respectively range near and below the FMQ and Pt-PtS buffers. This conclusion is further supported by independent thermodynamic calculations using the olivine-opx+MSS equilibrium (Figure 10E; Eggler and Lorand, 1993). The sulfide liquid line of descent in LCB is driven by the crystallization of MSS, which typically ranges from Fe-rich to Ni-rich with decreasing temperature (e.g., Craig and Kullerud, 1969; Fleet et al., 1993; Fleet and Pan, 1994; Ebel and Naldrett, 1996). Metal enrichment and S depletion characterize the sulfide liquid line of descent in LCB, where the final crystallization products are likely xSS or ISS (e.g., Ballhaus et al., 2001).

As a comparative test of the Ni-rich and Cu-poor compositions of sulfide liquids inferred from the orthopyroxenite vein sulfides, I use data for erupted LCB from Cape Vogel (Papua New Guinea; König et al., 2010), which contain 60±8 ppm Co, 345±94 ppm Ni, and 38±12 ppm Cu, for 10.2±0.2 wt% FeO_t and 16±3 wt% MgO with a Mg# of 0.73±0.03 (all 1σ, the cumulate rock "PNG14" is excluded). An average sulfide liquid composition is calculated in equilibrium with the Cape Vogel LCB using sulfide liquid/silicate melt partition coefficients for Fe, Co, Ni, and Cu (Gaetani and Grove, 1997) and the O solubility model in sulfide liquid of Kiseeva and Wood (2015), for fO_2 and fS_2 conditions inferred at atmospheric pressure, 1,300–1,340°C and $-1 \leq \Delta \log fO_2[FMQ] \leq 0$ (Eggler and Lorand, 1993; Mungall and Brenan, 2014). This calculation provides an average sulfide liquid composition of 30.54±0.05 wt% Fe, 0.2211±0.0005 wt% Co, 29.32±0.01 wt% Ni, 1.17±0.02 wt% Cu, and 0.35±0.01 wt% O (all 1σ) with S fixed at 38.40 wt% (average S data from (Fleet et al., 1993) and (Fleet and Pan, 1994)). This estimate agrees with earlier calculations based on orthopyroxenite vein sulfides, although the latter are more imprecise in nature given the wide compositional range of MSS therein (Figure 11C). Both calculations imply Ni-rich and Cu-poor compositions for sulfide liquids formed from magmas derived from spinel harzburgite sources, for instance in comparison with those calculated from lherzolite-derived primitive MORB, which contain only ~25 wt% Ni but up to ~8 wt% Cu (Kiseeva and Wood, 2015).

Note that it is important to find similar compositions for sulfide liquids calculated from MSS in orthopyroxenite veins, on the one hand, and from erupted LCB, on the other hand. Indeed, there is *a priori* no guarantee that the parental sulfide liquids formed in the LCB veins did not experience one or several immiscibility gaps before MSS crystallization, even those preserved as homogeneous globules. Liquid immiscibility in the Fe-Ni-Cu-S-O system has been suggested in pioneering field studies (e.g., Distler et al., 1986). However, more recent experimental works have shown that this process was extending below the MSS liquidus, but only for sulfide liquids with originally high ∑metal/S>1, and with the main involvement of a fractionating, Cu-rich phase (Ballhaus et al., 2001). For instance, there is no evidence for such liquid immiscibility gap in the ∑metal/S of homogeneous vein MSS, which stays in a narrow range of ca. 0.9–1 (Figure 7B; Ballhaus et al., 2001). Therefore, calculations of sulfide liquid compositions in equilibrium with Cape Vogel LCB confirm that immiscibility gaps unlikely altered the vein MSS compositions formed at least down to ~950°C (Supplementary Table S1).

Sulfur and precious metals in magmas derived from spinel harzburgite: Mantle source conditions

Estimates of the P-T-fO_2-fS_2 conditions and compositional range of the sulfide liquid line of descent in LCB has implications for the evolution of sulfur and precious metals in the spinel harzburgite sources of these magmas. First, it could be expected that these sources will not contain more

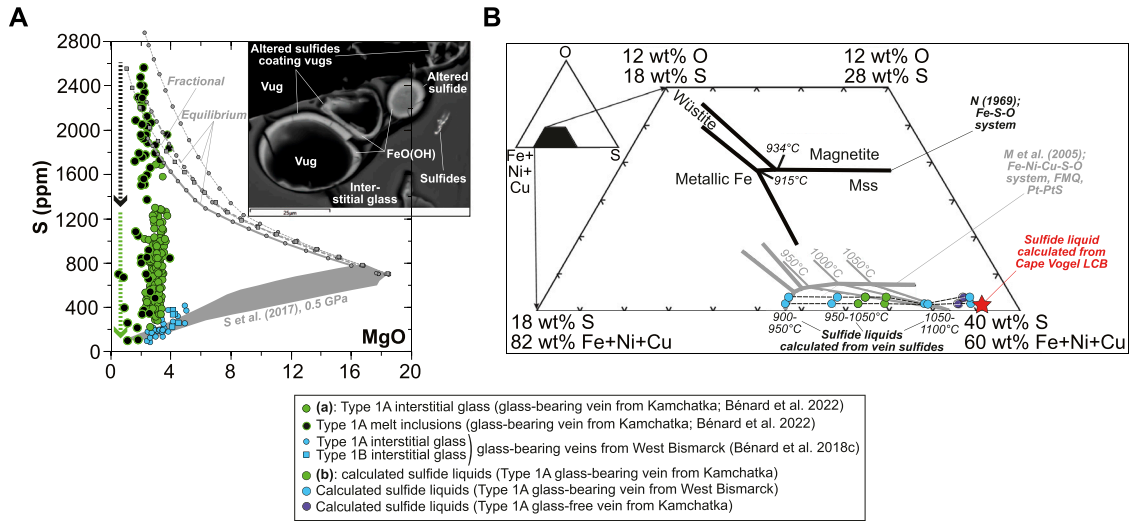

FIGURE 12
Sulfur saturation state and sulfide liquid phase relations inferred for Kamchatka and West Bismarck Type 1A veins. **(A)** S abundances measured by EPMA and SEM in vein MI and interstitial glass plotted against MgO (in wt%; Bénard et al., 2018c; Bénard et al., 2022). Data are compared with the liquid lines of descent of spinel harzburgite-derived melts at 1 GPa, calculated by Bénard et al. (2018c) with pMELTS. These models are either coupled with SCSS calculations using the model of Smythe et al. (2017) at 0.5 GPa to simulate sulfide-saturated conditions (gray field), or assume that all S remains dissolved in the silicate melt (i.e., sulfur is treated as a perfectly incompatible element) to simulate sulfide- or sulfate-undersaturated conditions (gray lines). The inset is a BSE image (SEM) illustrating the magmatic (sulfides in interstitial glass) and hydrothermal (vugs coated with sulfides altered into Fe oxyhydroxide) origins of vein sulfides (scale bar is 25 µm). **(B)** Projection of the LCB sulfide liquid estimates in a portion of the triangular Fe(±Ni, Cu)-S-O plane. Data are shown in comparison with experimental phase relations for the Fe-S-O system (black lines; Naldrett, 1969) and the Fe-Ni-Cu-S-O system (gray lines; Mungall et al., 2005). Sulfide liquids calculated from the compositions of the vein sulfides in this study (colored dots) and from the compositions of Cape Vogel LCB (red star; König et al., 2010) are shown (see text for details).

than ~50 ppm S and will record relatively low fS_2, given the observations in studies of spinel harzburgites (Luguet et al., 2007; Lorand et al., 2013). This stands, however, only when assuming that no metasomatism of the spinel harzburgite sources occurred, which can possibly involve oxidized, S-rich fluids or melts in a subduction zone setting (e.g., Bénard et al., 2018b).

Spinel harzburgites from Kamchatka and West Bismarck, which are the putative sources and/or residues formed in equilibrium with LCB, record $-0.5 \leq \Delta \log fO_2[FMQ] \leq +1.5$ (Bénard et al., 2018a; Bénard et al., 2018b; Bénard et al., 2018c). High-T fS_2 conditions during LCB and orthopyroxenite formation can be calculated at 0.5–1 GPa and 1,000–1,400°C, using Equation 6 in Mungall and Brenan (2014) and the $(Fe_2O_3)_t$ contents in silicate melts derived from pMELTS (Ghiorso et al., 2002) calculations for LCB differentiation (Figure 1A; Bénard et al., 2018c; Bénard et al., 2022). The results indicate that fS_2 at sulfide/sulfate saturation ranges from 1.6 to 3.9 bars at $\Delta \log fO_2[FMQ] = +1.5$ and from −1.3 to 1.1 bars (both in log units) at $\Delta \log fO_2[FMQ] = -1$. The estimated fS_2 range at relatively low fO_2 overlaps with the results based on the olivine-opx+MSS equilibrium for the veins (Figure 11E). In the first part of this study, it was shown that the parental LCB melts of the veins were originally equilibrated at $\Delta \log fO_2[FMQ] \sim +1.5$, allowing them to carry up to ~2,600 ppm S (opx-hosted MI data; Figures 1A,B; Bénard et al., 2022). Assuming that these relatively high fO_2 conditions were also prevalent during the partial melting events forming LCB, it is more likely that sulfides, alloys and platinum-group minerals (PGM) in their spinel harzburgite sources were partially consumed by the formation of these melts (see Mungall and Brenan, 2014 and references therein). Consequently, these calculations also imply that a dramatic drop in fS_2 conditions must have occurred during vein formation, which involved LCB melt fractionation and local fO_2 reduction during S^{6+}-Fe^{2+} redox exchange with the host mantle (Figure 1B; Bénard et al., 2022).

An originally sulfide-undersaturated state has been proposed for the formation of "second-stage" melts such as boninites (Hamlyn and Keays, 1986; Keays, 1995; Valetich et al., 2019). In the case of the orthopyroxenite veins in this study, a comparison of S abundances in opx-hosted MI and in the interstitial glass is indeed consistent with an originally sulfide-undersaturated state of the LCB melt intruding the sub-arc mantle (Figure 1A and Figure 12A; Bénard et al.,

2018c; Bénard et al., 2022). Intrusion and cooling caused saturation in S-bearing, hydrothermal fluids in the veins, shortly after (or concurrently with) the onset of magmatic sulfide formation in the derivative high-Mg# andesite and dacite (Figure 12A; Bénard et al., 2018c; Bénard et al., 2022). Caution must be taken, however, when extrapolating the original sulfide-undersaturated state of vein-forming LCB in the shallow sub-arc mantle (≤1.5 GPa; Bénard et al., 2017a; Bénard et al., 2018a) to source conditions because of the strong effect of pressure on S solubility in silicate melts (e.g., Mavrogenes and O'Neill, 1999; Moretti and Baker, 2008). However, much of the data collected on the Kamchatka and West Bismarck veins point towards original LCB melts produced by partial melting at relatively low-P conditions of ca. 1–1.5 GPa (Figure 10A; Bénard and Ionov, 2012; Bénard and Ionov, 2013; Bénard et al., 2018c; Bénard et al., 2022), suggesting at least that the decompression effect on S solubility between the sources and the final emplacement sites was minimal.

An elevated oxidation state ($\Delta\log fO_2$[FMQ]~+1.5) and sulfide undersaturation during partial melting of spinel harzburgite at low pressure, that is, in the theoretical stability field of Pt alloys (Mungall and Brenan, 2014), provides key conditions for the transport and concentration of sulfur and precious metals. The low degrees of melting inferred for spinel harzburgite melting (F≤5% at 1 Gpa and ≤1,380°C; Bénard et al., 2017a; Bénard et al., 2018c; Bénard et al., 2022) ensure a natural concentration process for S in primary LCB. On the basis of differentiation models for these magmas calculated by Bénard et al. (2018c), ~700 ppm S can be estimated in the primary melt (Figure 12A). This translates into ca. 7–35 ppm S in the spinel harzburgite sources when assuming F=1–5%. Note that for all these calculations, sulfur is assumed to be purely incompatible, which is consistent with the fact that this element is mainly dissolved as S^{6+}-bearing species in the original silicate melts (Figure 1B; Bénard et al., 2022). Sulfide-poor spinel harzburgites contain alloys and PGM (e.g., Lherz peridotites; Luguet et al., 2007), which can be partially destabilized at relatively high fO_2 conditions to be transported by the primary LCB melt (Mungall and Brenan, 2014). The presence of minor S^{2-} in this melt, even at $\Delta\log fO_2$[FMQ] ~+1.5 (Figure 1B), will also allow the formation of dissolved PGE-S^{2-} complexes, as it has been inferred for Pd or Ru (Laurenz et al., 2013; Mungall and Brenan, 2014). After being extracted from their spinel harzburgite sources, further dissolution of sulfides, alloys and PGM, either encapsulated in mantle minerals or located at grain boundaries, can occur in LCB during reactive melt percolation (Bénard and Ionov, 2012; Bénard and Ionov, 2013), for instance when these melts percolate through rocks with which they are out of equilibrium (e.g., lherzolites).

Sulfur and precious metals in magmas derived from spinel harzburgite: Mantle source signatures

Key signatures of harzburgite sources can be found in the major and trace metal compositions of vein sulfides, in particular their elevated Ni contents and sometimes very low Pd abundances with characteristic chondrite-normalized Pt/Pd>1 (Figures 8D, 9C, 10C). It has long been known that elevated Ni contents characterize sulfides formed from mafic and ultramafic magmas, with a negative relationship observed between Cu/(Cu+Ni) in sulfides and the MgO contents of the parental rocks (e.g., Naldrett and Cabri, 1976). At a given set of P-T conditions, the lherzolite-harzburgite source transition is not only accompanied by a drastic decrease in melt productivity (Hirschmann et al., 1999; Bénard et al., 2018c; Bénard et al., 2022), but also by a pronounced shift in primary melt compositions with increasing SiO_2 and MgO contents (Falloon and Danyushevsky, 2000; Bénard et al., 2018c; Bénard et al., 2022). Ni and Cu being respectively compatible and incompatible during mantle melting, the former element remains in the residues but not the latter, so that spinel harzburgites typically host higher Ni and lower Cu contents than spinel lherzolites (e.g., Lorand et al., 2013; Bénard et al., 2021). Furthermore, MgO-rich LCB are expected to be enriched in Ni in comparison with basalts, owing to the decrease in Ni partition coefficients between olivine and silicate melt with increasing MgO contents of the melt (e.g., Wang and Gaetani, 2008). These considerations explain why sulfide liquids derived from LCB are so enriched in Ni but not in Cu (Supplementary Table S1).

Low Pd contents at constant Pt levels, together with characteristic chondrite-normalized Pt/Pd>1 in some LCB sulfides must also be inherited from their spinel harzburgite sources (Figure 8D and Figure 9C). Knowing that Pd can concentrate in Cu-rich phases such as xSS or ISS (e.g., Liu and Brenan, 2015), it is important to note here that the variability in Pt/Pd is clearly unrelated to the presence of such phase, since homogeneous and heterogeneous globules in West Bismarck veins were analyzed in this study and both display this compositional feature (Figure 8D and Figure 9C). Instead, chondrite-normalized Pt/Pd>1 appears to be a characteristic signature of the West Bismarck vein sulfides (Figure 8 and Figure 9). So far, no MSS/sulfide liquid equilibration experiment has inferred any significant fractionation between Pd and Pt, with PPGE being always similarly incompatible in MSS (Fleet et al., 1993; Li et al., 1996; Ballhaus et al., 2001; Bockrath et al., 2004; Mungall et al., 2005; Ballhaus et al., 2006; Liu and Brenan, 2015). Therefore, variable Pt/Pd observed among Kamchatka and West Bismarck vein sulfides must reflect the PGE signatures of their parental sulfide liquids, since Pd is not significantly

hosted by any of the Pt alloys identified in this study (Supplementary Table S1). In addition, the sulfide liquid/silicate melt partition coefficients of Pt and Pd are similar, laying both near 10^5 (Mungall and Brenan, 2014), whereas the co-precipitation of Pd-free, Pt alloys can only lower Pt/Pd in coexisting MSS.

From the points discussed above, chondrite-normalized Pt/Pd ranging at ca. 10–30 in the West Bismarck vein sulfides must result from the equilibration of the original LCB silicate melts with Pd-depleted mantle rocks (Figure 8D). Such Pd depletion is a characteristic feature of many spinel harzburgites, either sampled as magma-hosted xenoliths or exhumed rocks in peridotite massifs (see Lorand et al., 2013 and references therein). Multiple melt extraction events forming spinel harzburgite residues are responsible for this Pd depletion, since this element is much more soluble than other PGE in silicate melts for a given set of P-T-*f* conditions (see Mungall and Brenan, 2014 and references therein). Though chondrite-normalized Pt/Pd>1 in magmatic MSS could thus be a key feature for formally identifying spinel harzburgite sources, fluctuations of this ratio among Kamchatka and West Bismarck LCB sulfides must also reflect the variable compositions of these sources, as can be expected from the wide, PGE compositional range of spinel harzburgites (see Lorand et al., 2013 and references therein). A possible origin for these Pt/Pd variations are Pd-rich sulfides armored in mantle-derived silicate or oxide grains, which do not react during the melting events forming spinel harzburgites, such as is the case for olivine under low-P and/or hydrous conditions at subduction zones (Gaetani and Grove, 1998).

Sulfur and precious metals in magmas derived from spinel harzburgite: Magma differentiation

The Ni-rich nature of sulfide melts formed from LCB has important implications for the evolution of precious metals when these magmas differentiate, for instance through crystal fractionation. Regarding phase relations, the first effect of the Ni-rich nature of the LCB sulfide liquids is to shift the cotectics close to the Fe(±Ni, Cu)-S join in the triangular Fe(±Ni, Cu)-S-O plane, for instance in comparison with the Fe-S-O system (Figure 12B; Naldrett, 1969; Mungall et al., 2005). A second effect is that the low O solubility resulting from high Ni contents places the estimated LCB sulfide liquids on the MSS side of the magnetite-MSS join (Figure 12B; Mungall et al., 2005; Fonseca et al., 2008), consistently with the paucity of primary oxides clearly associated with sulfides in the veins. It also appears that the estimated, sulfide liquid line of descent in LCB leads the final, xSS-forming products close to the metallic Fe-MSS join (Figure 12B). This is consistent with the identification of metallic Fe in vein vugs coated with altered, hydrothermal sulfides, while the presence of wüstite in the same fluid-derived spaces suggests that the eutectic of the Fe(±Ni, Cu)-S-O system was also reached (Figure 12B and Supplementary Figures S11, S12, S13). Finally, the trajectory of the sulfide liquid line of descent is parallel to the Fe(±Ni, Cu)-S join, which suggests that decreasing fO_2 and fS_2 during partial crystallization and fractionation, assuming a closed system, were mainly driven by cooling upon LCB intrusion in the sub-arc mantle.

The phase relations for the sulfide liquid line of descent in LCB described above provide further insights into the origin of oxides in the Kamchatka and West Bismarck veins. As mentioned above, some of the minute oxide grains found in association with late-stage xSS likely formed by cotectic precipitation, while those in the glass near the rims of MSS could be related to O diffusion out of the crystallizing sulfide liquid into the surrounding silicate melt (Figures 3H, 4B, 5F and Supplementary Figures S7, S8; Naldrett, 1969; Fonseca et al., 2008). The effects of the low O and high Ni contents in the sulfide liquids formed from LCB will be reinforced by the potential loss of O to the surrounding, high-Mg# andesite melts. Such rapid O loss will further contribute to moving the line of descent of these sulfide liquids on the MSS side of the MSS-magnetite join. Some of the magnetite grains identified on the rims of sulfides, however, could also be related to late-stage oxyhydration and FeO(OH) formation (Supplementary Figures S1, S2; Lorand, 1990). The common association of these alteration products with vugs and sulfide-rich vesicles (Figure 2H and Supplementary Figure S2; Bénard et al., 2022) suggests that they formed through a deuteric process involving high-T, hydrothermal fluids directly formed from LCB, most likely from ~1,000°C and shortly after (or concurrently with) the onset of magmatic MSS formation (Figure 10A and Figure 11C; Bénard et al., 2022).

During the ascent and emplacement of LCB as opx-rich dykes or sills, the decrease of fS_2 resulting from decompression and cooling leads to the precipitation of alloys together with sulfides, as observed in the orthopyroxenite veins (Figures 6, 9 and Supplementary Figures S9, S10; Mungall and Brenan, 2014). As calculations based on the fS_2 parameterization of Mungall and Brenan (2014) suggest (see above), decreasing temperature and Fe oxide contents of the silicate melts through fractionation are key factors controlling fS_2 at sulfide/sulfate saturation. Indeed, this parameter decreases by ca. 1.6–1.9 log units throughout the LCB liquid line of descent when assuming a fixed internal fO_2 buffer (e.g., either $\Delta\log fO_2$[FMQ]=−1 or $\Delta\log fO_2$[FMQ]=+1.5). This indicates that the "low-Fe" fractionation trend of LCB (see Arculus, 2003 and references therein) exerts a first-order control on decreasing fS_2 during cooling of these magmas. In the specific case of the Kamchatka and West Bismarck veins, it appears that fO_2 variations are also crucial in triggering sulfide and alloy

precipitation, since the originally S^{6+}-bearing LCB melt was locally converted into S^{2-}-bearing, high-Mg# andesite and dacite derivatives through redox reactions with the surrounding, Fe^{2+}-bearing mantle minerals (Figures 1A,B; Bénard et al., 2018c; Bénard et al., 2022). In the case of a local decrease in the LCB melt oxidation state from $\Delta\log fO_2$ [FMQ]=+1.5 to $\Delta\log fO_2$[FMQ]=−1 during intrusion, the resulting drop in fS_2 through cooling and differentiation could be as high as ca. 4.4–4.8 log units.

From the decreases of fO_2 and fS_2 during the formation of sulfides in LCB dykes and sills, it can be further inferred that PGE-bearing alloys must form from the onset of sulfide crystallization, or even at greater temperatures. This appears to be consistent with the widespread dissemination of alloys in the veins (Figures 6, 9 and Supplementary Figures S1, S9, S10), but also the variable Ir contents in vein sulfides; the greatest levels in this element appear in Fe-rich MSS formed at the highest temperatures along the sulfide liquid line of descent (Figure 8A). The orthopyroxenite vein sulfides are otherwise more enriched in Os and Ru than those found in high-Mg basaltic lavas from Kamchatka (Figure 8; Zelenski et al., 2017). Taken collectively, these pieces of evidence suggest that the original sulfide liquids were certainly more enriched in IPGE than what can be expected from the highly siderophile trace element patterns of most sulfide grains analyzed in this study. Even though direct formation of Os-Ir-Ru alloys from boninites has been suggested (Peck et al., 1992), the results in this study are also consistent with the precipitation of IPGE-bearing, Pt alloys before and during sulfide formation (Supplementary Table S1). The early saturation of LCB in such Pt alloys agrees with the nature of these phases when they are found in spinel harzburgites, which can be otherwise free of base metal sulfides (e.g., Pt-Ir±Os alloys; Luguet et al., 2007).

Other precious metals, such as Au and Ag, appear at relatively low levels in LCB, for instance in comparison with high-Mg basaltic lavas from Kamchatka (Figure 8; Zelenski et al., 2017). As in the case of Cu, this presumably results from the originally low abundances of Au and Ag in the depleted, spinel harzburgite sources of LCB (Figure 8A). These metals are expected to become enriched only in the very late-stage LCB sulfides (i.e., xSS or ISS), according to their partitioning behavior (Liu and Brenan, 2015); this point is supported by LA-ICPMS analyses of xSS-bearing, heterogeneous globules in this study (West Bismarck veins; Figure 8D).

Finally, it can also be expected from phase relations and the inferred fS_2 drop during LCB differentiation that a variety of metallic alloys and native metals will form down to the solidus temperatures of sulfide liquids derived from these magmas, and potentially further below (Figure 5, Figure 6 and Supplementary Figure S7). In addition, the separation of high-T, hydrothermal fluids from ~1,000°C, proven to be enriched in the volatile elements S and Cl (Bénard et al., 2018c; Bénard et al., 2022), can lead to the efficient solubilization of precious metals under the form of metal-Cl^- or metal-S^{2-} complexes to concentrate them in vugs or sulfide-rich vesicles (Supplementary Figures S10, S11, S12; Sullivan et al., 2022a; Sullivan et al., 2022b). Overall, the abrupt sulfide and alloy precipitation processes from low-S solubility, high-Mg# andesite and dacite melts formed by the differentiation of primary LCB, which chronologically match the formation of hydrothermal fluids (Figure 1A), allow the efficient capture of precious metals in localized, opx-rich zones.

Conclusion

In the first article, we have reported petrological data for a new, glass-bearing orthopyroxenite vein cutting a sub-arc mantle xenolith from Kamchatka. As similar veins from the West Bismarck arc (Papua New Guinea), this orthopyroxenite formed by cooling of parental melts (low-Ca boninite; LCB), which were originally produced by partial melting of spinel harzburgite sources at low pressure. Here I conducted a detailed petrological (textures and phase relations) and geochemical (major base metals and chalcophile and highly siderophile trace elements) study of sulfides and some of the metallic phases in orthopyroxenite veins from the two localities. The primary conclusions of this study are as follows:

1) Vein sulfides describe Ni and Cu enrichment trends (respectively from ~2 to ~30 wt% and from ~0.25 to ~2.5 wt %). Phase compositions vary from monosulfide solid solution (MSS; $(Fe, Ni)_{1-x}S$) to a ternary (Fe, Cu, Ni)S solid solution ("xSS"), which range between MSS and intermediate solid solution (ISS; $(Cu, Fe)S_{1-x}$), with decreasing temperatures of formation.
2) Fe-bearing oxides (most likely magnetite) are present in only small amounts in direct association with high-temperature MSS. These minerals appear in greater amounts when associated with late-stage xSS or sulfide-rich vesicles, while metallic Fe and wüstite are found in vugs formed by high-temperature, hydrothermal fluids. Pt alloys frequently appear in these vugs as well, but also on the surfaces of all types of sulfides; this metallic phase contain several percent of Rh, Au and Os, together with traces of Ir and Ru.
3) All sulfides have chondrite-normalized platinum-group element (PGE) patterns with elevated PPGE (Pt and Pd) relative to IPGE (Os, Ir and Ru) and Rh. A key systematic difference between Kamchatka and West Bismarck sulfides is the much lower Pd abundances in the latter setting than in the former with chondrite-normalized Pt/Pd of ca. 0.3-4 and ca. 10–30, respectively. The Fe-rich MSS formed at the highest temperatures are characterized by variable Ir negative

anomalies relative to Os and Ru; the two latter elements are commonly contained in greater amounts in LCB sulfides than in those from high-Mg basaltic lavas from Kamchatka.

4) Vein sulfides constitute the crystallization products of a sulfide liquid line of descent from Fe-rich MSS (ca. 1,050–1,100°C) to xSS (≤850°C) through Ni-rich MSS. Calculations suggest that the sulfides crystallized under oxygen and sulfur fugacity conditions (fO_2 and fS_2) down to one log unit below the fayalite-magnetite-quartz (FMQ) and close to the Pt-PtS buffers, respectively.
5) The estimated compositions of sulfide liquids formed from LCB are typically high in Ni but low in Cu (original atomic ∑metal/S~0.9) and will finally solidify either as xSS or ISS. The crystallization sequence of this sulfide liquid occurs at relatively low fS_2, which allows the formation of abundant PGE alloys. In this context, elevated Os and Ru but variable Ir abundances in vein sulfides can originate from the fractionation of cryptic, IPGE-bearing alloys (either Os-Ir-Ru or, more likely, IPGE-bearing Pt alloys). Alloy precipitation, therefore, begins at higher temperatures than sulfide formation and all along the sulfide liquid line of descent.
6) Low Pd in some of the sulfide liquids formed from LCB must reflect elevated Pt/Pd in their spinel harzburgite sources. This characteristic geochemical feature of some vein sulfides, as is the Ni-rich and Cu-poor nature of their parental sulfide liquids, originates from multiple episodes of melt extraction experienced by spinel harzburgite sources before the formation of LCB.
7) Combining the results of part 1 and part 2 of this study reveals that melts derived from spinel harzburgite sources can be originally oxidized ($\Delta\log fO_2$[FMQ]~+1.5) to carry up to ~2,600 ppm S, predominantly as S^{6+}-bearing species. As such, LCB can follow a sulfide-undersaturated evolution trend during decompression from their mantle sources to their final emplacement sites. Rapid cooling of LCB leads to the formation of orthopyroxenite dykes or sills, where the silicate melt fraction follows a low-Fe fractionation trend to produce derivative, high-Mg# andesite and dacite with low S solubility. In addition, S^{6+}-Fe^{2+} redox reactions with the host rocks can locally reduce the oxidation state of the fractionating melt down to $-1 \leq \Delta\log fO_2$[FMQ]≤ 0. High-temperature, S- and Cl-bearing hydrothermal fluids form from ~1,000°C, that is, shortly after (or concurrently with) the onset of sulfide liquid crystallization. The combination of a temperature drop, a low-Fe fractionation trend, and decreasing fO_2 result in a sharp fall of fS_2 within the orthopyroxenite, which, together with the formation of hydrothermal fluids and the low S solubility in LCB derivative melts, will lead to the local precipitation of abundant, magmatic and hydrothermal sulfides and alloys.

Data availability statement

The original contributions presented in the study are included in the article/Supplementary Material; further inquiries can be directed to the corresponding author.

Author contributions

AB acquired and treated all the data in this study and wrote the manuscript.

Funding

This work was supported by the Australian Research Council (DE120100513 to O Nebel and DP120104240 to RJ Arculus and O Nebel) at ANU. I have received funding from the European Union's Horizon 2020 research and innovation program under the Marie Skłodowska-Curie grant agreement 844795 at UNIL.

Acknowledgments

DA Ionov and RJ Arculus are thanked for providing access to the Kamchatka and West Bismarck samples respectively. R Rapp and JW Park provided assistance, respectively with EPMA and LA-ICPMS analyses at ANU. C De Meyer and A Demers-Roberge provided assistance with SEM analyses at UNIL.

Conflict of interest

The author declares that the research was conducted in the absence of any commercial or financial relationships that could be construed as a potential conflict of interest.

Publisher's note

All claims expressed in this article are solely those of the authors and do not necessarily represent those of their affiliated organizations, or those of the publisher, the editors, and the reviewers. Any product that may be evaluated in this article, or claim that may be made by its manufacturer, is not guaranteed or endorsed by the publisher.

Supplementary material

The Supplementary Material for this article can be found online at: https://www.frontiersin.org/articles/10.3389/feart.2022.868011/full#supplementary-material

SUPPLEMENTARY FIGURE S1
BSE images (SEM) and EDS spectra for the alteration rim (Fe oxyhydroxide) of a core sulfide in the glass-bearing vein from Kamchatka.

SUPPLEMENTARY FIGURE S2
BSE images (SEM) and EDS spectra for oxides (presumably magnetite) located in the alteration zones of rim and core sulfides in the glass-bearing vein from West Bismarck.

SUPPLEMENTARY FIGURE S3
Top: major element maps (EPMA) for a core sulfide in the glass-bearing vein from Kamchatka (Figures 3D–G). Scale bar is 200 µm, while the elements mapped are indicated in the bottom left corners of the images. BSE images (SEM) and EDS spectra for rim sulfides in this glass-bearing vein are shown below. Note that the y axis unit is counts per second per electronvolt (cps/eV) in the top EDS spectrum, whereas absolute counts are used for all other EDS spectra plotted in this study. Bottom: BSE images (SEM) and EDS spectra for rim and core sulfides in the glass-free vein from Kamchatka.

SUPPLEMENTARY FIGURE S4
BSE image (SEM) and EDS spectra for a MI-hosted sulfide in the glass-bearing vein from Kamchatka.

SUPPLEMENTARY FIGURE S5
Top: major element maps (EPMA) for a core sulfide in the glass-bearing vein from West Bismarck (Figures 4G–J). Scale bar is 100 µm, while the elements mapped are indicated in the top left corners of the images. BSE images (SEM) and EDS spectra for rim and core sulfides in this glass-bearing vein are shown below.

SUPPLEMENTARY FIGURE S6
BSE images and major element maps (SEM) for core sulfides in the glass-bearing veins from Kamchatka (left column) and West Bismarck (right column). The elements mapped are indicated in the top left corners of the images.

SUPPLEMENTARY FIGURE S7
BSE images (SEM) and EDS spectra for oxide inclusions (most likely magnetite and possibly wüstite) associated with 'cryptic' Cu-rich zones (presumably 'xSS') in rim sulfides from the glass-bearing vein from West Bismarck.

SUPPLEMENTARY FIGURE S8
BSE images (SEM) and EDS spectra for oxides (most likely magnetite and possibly wüstite) located in the interstitial glass near a rim sulfide from the glass-bearing vein from West Bismarck.

SUPPLEMENTARY FIGURE S9
BSE images (SEM) and EDS spectra for Pt alloys identified on sulfides in the glass-bearing vein from Kamchatka.

SUPPLEMENTARY FIGURE S10
BSE images (SEM) and EDS spectra for Pt alloys identified on and near sulfides in the glass bearing vein from West Bismarck.

SUPPLEMENTARY FIGURE S11
BSE images (SEM) and EDS spectra for metallic Fe identified in vugs from the glass-bearing vein from Kamchatka.

SUPPLEMENTARY FIGURE S12
BSE images (SEM) and EDS spectra for metallic Fe identified in vugs from the glass-bearing vein from West-Bismarck.

SUPPLEMENTARY FIGURE S13
BSE images (SEM) and EDS spectra for wüstite identified in vugs from the glass-bearing vein from West Bismarck.

References

Alt, J. C., Garrido, C. J., Shanks, W. C., III, Turchyn, A., Padrón-Navarta, J. A., Sánchez-Vizcaíno, V. L., et al. (2012). Recycling of water, carbon, and sulfur during subduction of serpentinites: A stable isotope study of cerro del almirez, Spain. *Earth Planet. Sci. Lett.* 327-328, 50–60. doi:10.1016/j.epsl.2012.01.029

Arculus, R. J. (2003). Use and abuse of the terms calcalkaline and calcalkalic. *J. Petrology* 44, 929–935. doi:10.1093/petrology/44.5.929

Arculus, R. J., and Powell, R. (1986). Source component mixing in the regions of arc magma generation. *J. Geophys. Res.* 91, 5913–5926. doi:10.1029/jb091ib06p05913

Ballhaus, C., Bockrath, C., Wohlgemuth-Ueberwasser, C., Laurenz, V., and Berndt, J. (2006). Fractionation of the noble metals by physical processes. *Contrib. Mineral. Pet.* 152, 667–684. doi:10.1007/s00410-006-0126-z

Ballhaus, C., Tredoux, M., and Späth, A. (2001). Phase relations in the Fe–Ni–Cu–PGE–S system at magmatic temperature and application to massive sulphide ores of the sudbury igneous complex*. *J. Petrology* 42, 1911–1926. doi:10.1093/petrology/42.10.1911

Barin, I. (1995). *Thermochemical data of pure substances*. Weinheim: Wiley-VCH Verlag GmbH, 1885.

Bédard, J. H. (1999). Petrogenesis of boninites from the Betts Cove ophiolite, Newfoundland, Canada: Identification of subducted source components. *J. Petrology* 40, 1853–1889. doi:10.1093/petroj/40.12.1853

Bénard, A., Arculus, R. J., Nebel, O., Ionov, D. A., and McAlpine, S. R. B. (2017a). Silica-enriched mantle sources of subalkaline picrite-boninite-andesite island arc magmas. *Geochim. Cosmochim. Acta* 199, 287–303. doi:10.1016/j.gca.2016.09.030

Bénard, A., and Ionov, D. A. (2012). A new petrogenetic model for low-Ca boninites: Evidence from veined sub-arc xenoliths on melt-mantle interaction and melt fractionation. *Geochem. Geophys. Geosyst.* 13. doi:10.1029/2012GC004145

Bénard, A., Klimm, K., Woodland, A. B., Arculus, R. J., Wilke, M., Botcharnikov, R. E., et al. (2018b). Oxidising agents in sub-arc mantle melts link slab devolatilisation and arc magmas. *Nat. Commun.* 9, 3500. doi:10.1038/s41467-018-05804-2

Bénard, A., Koga, K. T., Shimizu, N., Kendrick, M. A., Ionov, D. A., Nebel, O., et al. (2017b). Chlorine and fluorine partition coefficients and abundances in sub-arc mantle xenoliths (Kamchatka, Russia): Implications for melt generation and volatile recycling processes in subduction zones. *Geochim. Cosmochim. Acta* 199, 324–350. doi:10.1016/j.gca.2016.10.035

Bénard, A., Le Losq, C., Müntener, O., Robyr, M., Nebel, O., Arculus, R. J., et al. (2022). Spinel harzburgite-derived silicate melts forming sulfide-bearing orthopyroxenite in the lithosphere. Part 1: Partition coefficients and volatile evolution accompanying fluid- and redox-induced sulfide formation. *Front. Earth Sci. (Lausanne).* 10. doi:10.3389/feart.2022.867979

Bénard, A., Le Losq, C., Nebel, O., and Arculus, R. J. (2018c). Low-Ca boninite formation by second-stage melting of spinel harzburgite residues at mature subduction zones: New evidence from veined mantle xenoliths from the west Bismarck arc. *Contrib. Mineral. Pet.* 173, 105. doi:10.1007/s00410-018-1526-6

Bénard, A., Müntener, O., Pilet, S., Arculus, R. J., and Nebel, O. (2021). Silica-rich spinel harzburgite residues formed by fractional hybridization-melting of the intra-oceanic supra-subduction zone mantle: New evidence from TUBAF seamount peridotites. *Geochim. Cosmochim. Acta* 293, 477–506. doi:10.1016/j.gca.2020.11.001

Bénard, A., Nebel, O., Ionov, D. A., Arculus, R. J., Shimizu, N., and Métrich, N. (2016). Primary silica-rich picrite and high-Ca boninite melt inclusions in pyroxenite veins from the Kamchatka sub-arc mantle. *J. Petrol.* 57, 1955–1982. doi:10.1093/petrology/egw066

Bénard, A., Palle, S., Doucet, L. S., and Ionov, D. A. (2011). Three-dimensional imaging of sulfides in silicate rocks at submicron resolution with multiphoton microscopy. *Microsc. Microanal.* 17, 937–943. doi:10.1017/s1431927611011883

Bénard, A., Woodland, A. B., Arculus, R. J., Nebel, O., and McAlpine, S. R. B. (2018a). Variation in sub-arc mantle oxygen fugacity during partial melting recorded in refractory peridotite xenoliths from the West Bismarck Arc. *Chem. Geol.* 486, 16–30. doi:10.1016/j.chemgeo.2018.03.004

Bénard, A., and Ionov, D. A. (2013). Melt- and fluid-rock interaction in supra-subduction lithospheric mantle: Evidence from andesite-hosted veined peridotite xenoliths. *J. Petrology* 54, 2339–2378. doi:10.1093/petrology/egt050

Berry, A. J., Stewart, G. A., O'Neill, H. StC., Mallmann, G., and Mosselmans, J. F. W. (2018). A re-assessment of the oxidation state of iron in MORB glasses. *Earth Planet. Sci. Lett.* 483, 114–123. doi:10.1016/j.epsl.2017.11.032

Bockrath, C., Ballhaus, C., and Holzheid, A. (2004). Fractionation of the platinum group elements during mantle melting. *Science* 305, 1951–1953. doi:10.1126/science.1100160

Botcharnikov, R. E., Linnen, R. L., Wilke, M., Holtz, F., Jugo, P. J., and Berndt, J. (2011). High gold concentrations in sulphide-bearing magma under oxidizing conditions. *Nat. Geosci.* 4, 112–115. doi:10.1038/NGEO1042

Brenan, J. M., McDonough, W. F., and Ash, R. (2005). An experimental study of the solubility and partitioning of iridium, osmium and gold between olivine and silicate melt. *Earth Planet. Sci. Lett.* 237, 855–872. doi:10.1016/j.epsl.2005.06.051

Brounce, M., Kelley, K. A., Cottrell, E., and Reagan, M. K. (2015). Temporal evolution of mantle wedge oxygen fugacity during subduction initiation. *Geology* 43, 775–778. doi:10.1130/g36742.1

Brounce, M., Reagan, M. K., Kelley, K. A., Cottrell, E., Shimizu, K., and Almeev, R. (2021). Covariation of slab tracers, volatiles, and oxidation during subduction initiation. *Geochem. Geophys. Geosyst.* 22. doi:10.1029/2021GC009823

Cameron, W. E., McCulloch, M. T., and Walker, D. A. (1983). Boninite petrogenesis: Chemical and Nd-Sr isotopic constraints. *Earth Planet. Sci. Lett.* 65, 75–89. doi:10.1016/0012-821x(83)90191-7

Cooper, L. B., Plank, T., Arculus, R. J., Hauri, E. H., Hall, P. S., and Parman, S. W. (2010). High-Ca boninites from the active Tonga Arc. *J. Geophys. Res.* 115, B10206. doi:10.1029/2009JB006367

Coulthard, D. A., Jr, Reagan, M. K., Shimizu, K., Bindeman, I. N., Brounce, M., Almeev, R. R., et al. (2021). Magma source evolution following subduction initiation: Evidence from the element concentrations, stable isotope ratios, and water contents of volcanic glasses from the Bonin forearc (IODP Expedition 352). *Geochem. Geophys. Geosyst.* 22. doi:10.1029/2020gc009054

Craig, J. R., and Kullerud, G. (1969). Phase relations in the Fe-Ni-Cu-S system and their application to magmatic ore deposits. *Econ. Geol.* 4, 344–358.

Crawford, A. J., Falloon, T. J., and Green, D. H. (1989). "Classification, petrogenesis and tectonic setting of boninites," in *Boninites and related rocks*. Editor A. J. Crawford (London: Unwin Hyman), 1–49.

Dale, C. W., Macpherson, C. G., Pearson, D. G., Hammond, S. J., and Arculus, R. J. (2012). Inter-element fractionation of highly-siderophile elements in the Tonga Arc due to flux melting of a depleted source. *Geochim. Cosmochim. Acta* 89, 202–225. doi:10.1016/j.gca.2012.03.025

Debret, B., and Sverjensky, D. A. (2017). Highly oxidising fluids generated during serpentinite breakdown in subduction zones. *Sci. Rep.* 7, 10351. doi:10.1038/s41598-017-09626-y

Distler, V. V., Genkin, A. D., and Dyuzhikov, O. A. (1986). "Sulfide petrology and Genesis of copper-nickel ore deposits," in *Geology and metallogeny of copper deposits*. Editors G. H. Friedrich, A. D. Genkin, A. J. Naldrett, J. D. Ridge, R. H. Sillitoe, and F. M. Vokes (Berlin: Springer), 111–123.

Duran, C. J., Barnes, S. J., Mansur, E. T., Dare, S. A. S., Bédard, L. P., and Sluzhenikin, S. F. (2020). Magnetite chemistry by LA-ICP-MS records sulfide fractional crystallization in massive nickel-copper-platinum group element ores from the norilsk-talnakh mining district (siberia, Russia): Implications for trace element partitioning into magnetite. *Econ. Geol.* 115, 1245–1266. doi:10.5382/econgeo.4742

Ebel, D. S., and Naldrett, A. J. (1996). Fractional crystallization of sulfide ore liquids at high temperature. *Econ. Geol.* 91, 607–621. doi:10.2113/gsecongeo.91.3.607

Eggler, D. H., and Lorand, J. P. (1993). Mantle sulfide geobarometry. *Geochim. Cosmochim. Acta* 57, 2213–2222. doi:10.1016/0016-7037(93)90563-c

Evans, K. A., Elburg, M. A., and Kamenetsky, V. S. (2012). Oxidation state of subarc mantle. *Geology* 40, 783–786. doi:10.1130/g33037.1

Falloon, T. J., and Danyushevsky, L. V. (2000). Melting of refractory mantle at 1.5, 2 and 2.5 GPa under anhydrous and H_2O-undersaturated conditions: Implications for the petrogenesis of high-Ca boninites and the influence of subduction components on mantle melting. *J. Petrology* 41, 257–283. doi:10.1093/petrology/41.2.257

Fleet, M. E. (2006). Phase equilibria at high temperatures. *Rev. Mineral. Geochem.* 61, 365–419. doi:10.2138/rmg.2006.61.7

Fleet, M. E., Chryssoulis, S. L., Stone, W. E., and Weisener, C. G. (1993). Partitioning of platinum-group elements and Au in the Fe-Ni-Cu-S system: Experiments on the fractional crystallization of sulfide melt. *Contr. Mineral. Pet.* 115, 36–44. doi:10.1007/bf00712976

Fleet, M. E., and Pan, Y. (1994). Fractional crystallization of anhydrous sulfide liquid in the system Fe-Ni-Cu-S, with application to magmatic sulfide deposits. *Geochim. Cosmochim. Acta* 58, 3369–3377. doi:10.1016/0016-7037(94)90092-2

Foden, J., Sossi, P. A., and Nebel, O. (2018). Controls on the iron isotopic composition of global arc magmas. *Earth Planet. Sci. Lett.* 494, 190–201. doi:10.1016/j.epsl.2018.04.039

Fonseca, R. O. C., Campbell, I. H., O'Neill, H. StC., and Fitzgerald, J. D. (2008). Oxygen solubility and speciation in sulphide-rich mattes. *Geochim. Cosmochim. Acta* 72, 2619–2635. doi:10.1016/j.gca.2008.03.009

Fonseca, R. O. C., Mallmann, G., O'Neill HStCand Campbell, I. H. (2007). How chalcophile is rhenium? An experimental study of the solubility of Re in sulphide mattes. *Earth Planet. Sci. Lett.* 260, 537–548. doi:10.1016/j.epsl.2007.06.012

Gaetani, G. A., and Grove, T. L. (1997). Partitioning of moderately siderophile elements among olivine, silicate melt, and sulfide melt: Constraints on core formation in the Earth and Mars. *Geochim. Cosmochim. Acta* 61, 1829–1846. doi:10.1016/s0016-7037(97)00033-1

Gaetani, G. A., and Grove, T. L. (1998). The influence of water on melting of mantle peridotite. *Contributions Mineralogy Petrology* 131, 323–346. doi:10.1007/s004100050396

Ghiorso, M. S., Hirschmann, M. M., Reiners, P. W., and Kress, V. C. (2002). The pMELTS: A revision of MELTS for improved calculation of phase relations and major element partitioning related to partial melting of the mantle to 3 GPa. *Geochem. Geophys. Geosyst.* 2002, 1–35. doi:10.1029/2001GC000217

Guillong, M., Danyushevsky, L. V., Walle, M., and Raveggi, M. (2011). The effect of quadrupole ICPMS interface and ion lens design on argide formation. Implications for LA-ICPMS analysis of PGE's in geological samples. *J. Anal. At. Spectrom.* 26, 1401–1407. doi:10.1039/c1ja10035a

Hamlyn, P. R., and Keays, R. R. (1986). Sulfur saturation and second-stage melts: Application to the Bushveld platinum metal deposits. *Econ. Geol.* 81, 1431–1445. doi:10.2113/gsecongeo.81.6.1431

Hickey, R. L., and Frey, F. A. (1982). Geochemical characteristics of boninite series volcanics: Implications for their source. *Geochim. Cosmochim. Acta* 46, 2099–2115. doi:10.1016/0016-7037(82)90188-0

Hirschmann, M. M., Asimow, P. D., Ghiorso, M. S., and Stolper, E. M. (1999). Calculation of peridotite partial melting from thermodynamic models of minerals and melts. III. Controls on isobaric melt production and the effect of water on melt production. *J. Petrology* 40, 831–851. doi:10.1093/petroj/40.5.831

Ionov, D. A. (2010). Petrology of mantle wedge lithosphere: New data on supra-subduction zone peridotite xenoliths from the andesitic Avacha volcano, Kamchatka. *J. Petrology* 51, 327–361. doi:10.1093/petrology/egp090

Jégo, S., and Dasgupta, R. (2013). Fluid-present melting of sulfide-bearing ocean-crust: Experimental constraints on the transport of sulfur from subducting slab to mantle wedge. *Geochim. Cosmochim. Acta* 110, 106–134. doi:10.1016/j.gca.2013.02.011

Jégo, S., and Dasgupta, R. (2014). The fate of sulfur during fluid-present melting of subducting basaltic crust at variable oxygen fugacity. *J. Petrology* 55, 1019–1050. doi:10.1093/petrology/egu016

Jenner, G. A. (1981). Geochemistry of high-Mg andesites from Cape Vogel, Papua New Guinea. *Chem. Geol.* 33, 307–332. doi:10.1016/0009-2541(81)90106-6

Jochum, K. P., Weis, U., Stoll, B., Kuzmin, D., Yang, Q., Raczek, I., et al. (2011). Determination of reference values for NIST SRM 610-617 glasses following ISO guidelines. *Geostand. Geoanal. Res.* 35, 397–429. doi:10.1111/j.1751-908x.2011.00120.x

Jugo, P. J., Wilke, M., and Botcharnikov, R. E. (2010). Sulfur K-edge XANES analysis of natural and synthetic basaltic glasses: Implications for S speciation and S content as function of oxygen fugacity. *Geochim. Cosmochim. Acta* 74, 5926–5938. doi:10.1016/j.gca.2010.07.022

Kamenetsky, V. S., Park, J. W., Mungall, J. E., Pushkarev, E. V., Ivanov, A. V., Kamenetsky, M. B., et al. (2015). Crystallization of platinum-group minerals from silicate melts: Evidence from Cr-spinel-hosted inclusions in volcanic rocks. *Geology* 43, 903–906. doi:10.1130/g37052.1

Kamenetsky, V. S., Sobolev, A. V., Eggins, S. M., Crawford, A. J., and Arculus, R. J. (2002). Olivine-enriched melt inclusions in chromites from low-Ca boninites, Cape Vogel, Papua New Guinea: Evidence for ultramafic primary magma, refractory mantle source and enriched components. *Chem. Geol.* 183, 287–303. doi:10.1016/s0009-2541(01)00380-1

Keays, R. R. (1995). The role of komatiitic and picritic magmatism and S-saturation in the formation of ore deposits. *Lithos* 34, 1–18. doi:10.1016/0024-4937(95)90003-9

Kelley, K. A., and Cottrell, E. (2009). Water and the oxidation state of subduction zone magmas. *Science* 325, 605–607. doi:10.1126/science.1174156

Kessel, R., Schmidt, M. W., Ulmer, P., and Pettke, T. (2005). Trace element signature of subduction-zone fluids, melts and supercritical liquids at 120-180 km depth. *Nature* 437, 724–727. doi:10.1038/nature03971

Kiseeva, E. S., and Wood, B. J. (2015). The effects of composition and temperature on chalcophile and lithophile element partitioning into magmatic sulphides. *Earth Planet. Sci. Lett.* 424, 280–294. doi:10.1016/j.epsl.2015.05.012

Klimm, K., Kohn, S. C., and Botcharnikov, R. E. (2012). The dissolution mechanism of sulphur in silicate melts. II: Solubility and speciation of sulphur in silicate melts as a function of fO_2. *Chem. Geol.* 322-323, 250–267. doi:10.1016/j.chemgeo.2012.04.028

Klingenberg, B. M. E. T., and Kushiro, I. (1996). Melting of a chromite-bearing harzburgite and generation of boninitic melts at low pressures under controlled oxygen fugacity. *Lithos* 37, 1–14. doi:10.1016/0024-4937(95)00025-9

König, S., Münker, C., Schuth, S., Luguet, A., Elis Hoffmann, J., and Kuduon, J. (2010). Boninites as windows into trace element mobility in subduction zones. *Geochim. Cosmochim. Acta* 74, 684–704. doi:10.1016/j.gca.2009.10.011

Kullerud, G., Yund, R. A., and Moh, G. H. (1969). Phase relation in the Cu-Fe-Ni, Cu-Ni-S and Fe-Ni-S systems. *Econ. Geol.* 4, 323–343.

Laurenz, V., Fonseca, R. O. C., Ballhaus, C., Jochum, K. P., Heuser, A., and Sylvester, P. J. (2013). The solubility of palladium and ruthenium in picritic melts: 2. The effect of sulfur. *Geochim. Cosmochim. Acta* 108, 172–183. doi:10.1016/j.gca.2013.01.013

Le Bas, M. J. (2000). IUGS reclassification of the high-Mg and picritic volcanic rocks. *J. Petrology* 41, 1467–1470. doi:10.1093/petrology/41.10.1467

Li, C., Barnes, S. J., Makovicky, E., Rose-Hansen, J., and Makovicky, M. (1996). Partitioning of nickel, copper, iridium, rhenium, platinum and palladium between monosulfide solid solution and sulfide liquid: Effects of composition and temperature. *Geochim. Cosmochim. Acta* 60, 1231–1238. doi:10.1016/0016-7037(96)00009-9

Li, J. L., Schwarzenbach, E. M., Timm, J., Ague, J. J., Huang, F., Gao, J., et al. (2020). Uncovering and quantifying the subduction zone sulfur cycle from the slab perspective. *Nat. Commun.* 11, 514. doi:10.1038/s41467-019-14110-4

Liu, Y., and Brenan, J. (2015). Partitioning of platinum-group elements (PGE) and chalcogens (Se, Te, As, Sb, Bi) between monosulfide-solid solution (MSS), intermediate solid solution (ISS) and sulfide liquid at controlled fO_2-fS_2 conditions. *Geochim. Cosmochim. Acta* 159, 139–161. doi:10.1016/j.gca.2015.03.021

Longerich, H. P., Jackson, S. E., and Günther, D. (1996). Inter-laboratory note. Laser ablation inductively coupled plasma mass spectrometric transient signal data acquisition and analyte concentration calculation. *J. Anal. At. Spectrom.* 11, 899–904. doi:10.1039/ja9961100899

Lorand, J. P. (1989). Mineralogy and chemistry of Cu-Fe-Ni sulfides in orogenic-type spinel peridotite bodies from Ariege (Northeastern Pyrenees, France). *Contr. Mineral. Pet.* 103, 335–345. doi:10.1007/bf00402920

Lorand, J. P. (1990). Are spinel lherzolite xenoliths representative of the abundance of sulfur in the upper mantle? *Geochim. Cosmochim. Acta* 54, 1487–1492. doi:10.1016/0016-7037(90)90173-i

Lorand, J. P., Luguet, A., and Alard, O. (2013). Platinum-group element systematics and petrogenetic processing of the continental upper mantle: A review. *Lithos* 164-167, 2–21. doi:10.1016/j.lithos.2012.08.017

Luguet, A., Shirey, S. B., Lorand, J. P., Horan, M. F., and Carlson, R. W. (2007). Residual platinum-group minerals from highly depleted harzburgites of the Lherz massif (France) and their role in HSE fractionation of the mantle. *Geochim. Cosmochim. Acta* 71, 3082–3097. doi:10.1016/j.gca.2007.04.011

Maurice, J., Bolfan-Casanova, N., Demouchy, S., Chauvigne, P., Schiavi, F., and Debret, B. (2020). The intrinsic nature of antigorite breakdown at 3 GPa: Experimental constraints on redox conditions of serpentinite dehydration in subduction zones. *Contrib. Mineral. Pet.* 175, 94–116. doi:10.1007/s00410-020-01731-y

Mavrogenes, J. A., and O'Neill, H. StC. (1999). The relative effects of pressure, temperature and oxygen fugacity on the solubility of sulfide in mafic magmas. *Geochim. Cosmochim. Acta* 63, 1173–1180. doi:10.1016/s0016-7037(98)00289-0

McDonough, W. F., and Sun, S. S. (1995). The composition of the Earth. *Chem. Geol.* 120, 223–253. doi:10.1016/0009-2541(94)00140-4

Moretti, R., and Baker, D. R. (2008). Modeling the interplay of fO_2 and fS_2 along the FeS-silicate melt equilibrium. *Chem. Geol.* 256, 286–298. doi:10.1016/j.chemgeo.2008.06.055

Mungall, J. E. (2007). Crystallization of magmatic sulfides: An empirical model and application to Sudbury ores. *Geochim. Cosmochim. Acta* 71, 2809–2819. doi:10.1016/j.gca.2007.03.026

Mungall, J. E., Andews, D. R. A., Cabri, L. J., Sylvester, P. J., and Tubrett, M. (2005). Partitioning of Cu, Ni, Au, and platinum-group elements between monosulfide solid solution and sulfide melt under controlled oxygen and sulfur fugacities. *Geochim. Cosmochim. Acta* 69, 4349–4360. doi:10.1016/j.gca.2004.11.025

Mungall, J. E., and Brenan, J. M. (2014). Partitioning of platinum-group elements and Au between sulfide liquid and basalt and the origins of mantle-crust fractionation of the chalcophile elements. *Geochim. Cosmochim. Acta* 125, 265–289. doi:10.1016/j.gca.2013.10.002

Naldrett, A. J. (1969). A portion of the system Fe-S-O between 900 and 1080°C and its application to sulfide ore magmas. *J. Petrology* 10, 171–201. doi:10.1093/petrology/10.2.171

Naldrett, A. J., and Cabri, L. J. (1976). Ultramafic and related mafic rocks: Their classification and Genesis with special reference to the concentration of nickel sulfides and platinum-group elements. *Econ. Geol.* 71, 1131–1158. doi:10.2113/gsecongeo.71.7.1131

Nebel, O., Sossi, P. A., Bénard, A., Wille, M., Vroon, P. Z., and Arculus, R. J. (2015). Redox-variability and controls in subduction zones from an iron-isotope perspective. *Earth Planet. Sci. Lett.* 432, 142–151. doi:10.1016/j.epsl.2015.09.036

Palme, H., and O'Neill, H. StC. (2014). "Cosmochemical estimates of mantle composition," in *Treatise on geochemistry*. Editors H. Holland and K. Turekian. 2nd edn. (Amsterdam: Elsevier), 1–39.

Park, J. W., Campbell, I. H., and Arculus, R. J. (2013). Platinum-alloy and sulfur saturation in an arc-related basalt to rhyolite suite: Evidence from the Pual Ridge lavas, the Eastern Manus Basin. *Geochim. Cosmochim. Acta* 101, 76–95. doi:10.1016/j.gca.2012.10.001

Park, J. W., Campbell, I. H., and Eggins, S. M. (2012). Enrichment of Rh, Ru, Ir and Os in Cr spinels from oxidized magmas: Evidence from the Ambae volcano, Vanuatu. *Geochim. Cosmochim. Acta* 78, 28–50. doi:10.1016/j.gca.2011.11.018

Parman, S. W., and Grove, T. L. (2004). Harzburgite melting with and without H_2O: Experimental data and predictive modelling. *J. Geophys. Res.* 109. doi:10.1029/2003JB002566

Pearce, J. A., and Reagan, M. K. (2019). Identification, classification, and interpretation of boninites from Anthropocene to Eoarchean using Si-Mg-Ti systematics. *Geosphere* 15, 1008–1037. doi:10.1130/ges01661.1

Peck, D. C., Keays, R. R., and Ford, R. J. (1992). Direct crystallization of refractory platinum-group element alloys from boninitic magmas: Evidence from Western Tasmania. *Aust. J. Earth Sci.* 39, 373–387. doi:10.1080/08120099208728031

Peregoedova, A., and Ohnenstetter, M. (2002). Collectors of Pt, Pd and Rh in a S-poor Fe-Ni-Cu sulfide system at 760°C: Experimental data and application to ore deposits. *Can. Mineralogist* 40, 527–561. doi:10.2113/gscanmin.40.2.527

Piccoli, F., Hermann, J., Pettke, T., Connolly, J. A. D., Kempf, E. D., and Vieira Duarte, J. F. (2019). Subducting serpentinites release reduced, not oxidized, aqueous fluids. *Sci. Rep.* 9, 19573. doi:10.1038/s41598-019-55944-8

Prouteau, G., and Scaillet, B. (2012). Experimental constraints on sulphur behaviour in subduction zones: Implications for TTG and adakite production and the global sulphur cycle since the Archean. *J. Petrology* 54, 183–213. doi:10.1093/petrology/egs067

Reagan, M. K., Ishizuka, O., Stern, R. J., Kelley, K. A., Ohara, Y., Blichert-Toft, J., et al. (2009). Fore-arc basalts and subduction initiation in the Izu-Bonin-Mariana system. *Geochem. Geophys. Geosyst.* 11. doi:10.1029/2009GC002871

Salters, V. J. M., and Stracke, A. (2004). Composition of the depleted mantle. *Geochem. Geophys. Geosyst.* 5. doi:10.1029/2003GC000597

Smythe, D., Wood, B. J., and Kiseeva, E. S. (2017). The S content of silicate melts at sulfide saturation: New experiments and a model incorporating the effects of sulfide composition. *Am. Mineral.* 102, 795–803. doi:10.2138/am-2017-5800ccby

Sobolev, A. V., and Chaussidon, M. (1996). H_2O concentrations in primary melts from supra-subduction zones and mid-ocean ridges: Implications for H_2O storage and recycling in the mantle. *Earth Planet. Sci. Lett.* 137, 45–55. doi:10.1016/0012-821x(95)00203-o

Sullivan, N. A., Zajacz, Z., Brenan, J. M., Hinde, J. C., Tsay, A., and Yin, Y. (2022a). The solubility of gold and palladium in magmatic brines: Implications for PGE enrichment in mafic-ultramafic and porphyry environments. *Geochim. Cosmochim. Acta* 316, 230–252. doi:10.1016/j.gca.2021.09.010

Sullivan, N. A., Zajacz, Z., Brenan, J. M., and Tsay, A. (2022b). The solubility of platinum in magmatic brines: Insights into the mobility of PGE in ore-forming environments. *Geochim. Cosmochim. Acta* 316, 253–272. doi:10.1016/j.gca.2021.09.014

Sylvester, P. J., and Eggins, S. M. (1997). Analysis of Re, Au, Pd, Pt and Rh in NIST glass certified reference materials and natural basalt glasses by laser ablation ICP-MS. *Geostand. Geoanal. Res.* 21, 215–229. doi:10.1111/j.1751-908x.1997.tb00672.x

Taylor, R. N., Nesbitt, R. W., Vidal, P., Harmon, R. S., Auvray, B., and Croudace, I. W. (1994). Mineralogy, chemistry, and Genesis of the boninite series volcanics, Chichijima, Bonin islands, Japan. *J. Petrology* 35, 577–617. doi:10.1093/petrology/35.3.577

Tomkins, A. G., and Evans, K. A. (2015). Separate zones of sulfate and sulfide release from subducted mafic oceanic crust. *Earth Planet. Sci. Lett.* 428, 73–83. doi:10.1016/j.epsl.2015.07.028

Valetich, M. J., Mavrogenes, J., Arculus, R. J., and Umino, S. (2019). Evolution of chalcophile elements in the magmas of the Bonin Islands. *Chem. Geol.* 508, 234–249. doi:10.1016/j.chemgeo.2018.07.011

Vaughan, D. J., and Craig, J. R. (1978). *Mineral chemistry of metal sulfides*. Cambridge: Cambridge University Press, 493.

Wallace, P. J. (2005). Volatiles in subduction zone magmas: Concentrations and fluxes based on melt inclusion and volcanic gas data. *J. Volcanol. Geotherm. Res.* 140, 217–240. doi:10.1016/j.jvolgeores.2004.07.023

Wang, Z., and Gaetani, G. A. (2008). Partitioning of Ni between olivine and siliceous eclogite partial melt: Experimental constraints on the mantle source of Hawaiian basalts. *Contrib. Mineral. Pet.* 156, 661–678. doi:10.1007/s00410-008-0308-y

Woodland, S. J., Pearson, D. G., and Thirlwall, M. F. (2002). A platinum group element and Re-Os isotope investigation of siderophile element recycling in subduction zones: Comparison of Grenada, Lesser Antilles arc, and the Izu-Bonin arc. *J. Petrology* 43, 171–198. doi:10.1093/petrology/43.1.171

Zelenski, M., Kamenetsky, V. S., Mavrogenes, J. A., Danyushevsky, L. V., Matveev, D., and Gurenko, A. A. (2017). Platinum-group elements and gold in sulfide melts from modern arc basalt (Tolbachik volcano, Kamchatka). *Lithos* 290-291, 172–188. doi:10.1016/j.lithos.2017.08.012

Zhang, Z., and Hirschmann, M. M. (2016). Experimental constraints on mantle sulfide melting up to 8 GPa. *Am. Mineral.* 101, 181–192. doi:10.2138/am-2016-5308